SIMULATION OF PLASTIC DEFORMATION IN A TWO-DIMENSIONAL ATOMIC GLASS BY MOLECULAR DYNAMICS - IV

D. Deng [1], A.S. Argon, and S. Yip

Massachusetts Institute of Technology, Cambridge, 02139

U.S.A.

Abstract

Plastic deformation in a structurally well-relaxed two-dimensional atomic glass was simulated by a computer molecular dynamics approach. The simulation, which was carried through yielding and to substantial plastic strains, demonstrated that the principal mechanism of plastic strain production is by local partially dilatant shear transformations nucleated preferentially in the boundaries of liquid-like material separating the small quasi-ordered domains that form when the glass is well relaxed. Under imposed forward shear strain increments, local shear transformations in atomic clusters were found to be mostly in the same direction as the applied stress. There were, however, substantial levels of shear transformations in other random directions, including many opposed to the applied stress. In all instances, however, nucleation of shear transformations reduced the Gibbs free energy monotonically, which is governed largely by

[1] On leave from the Institute for Precious Metals in Kunming, Yunan Province, China.

the locked-in excess enthalpies of the glassy state. At shear strains above 15%, localization of shear into bands was observed to begin. This steadily intensified and formed well-defined sharp shear bands into which all the shear strain became concentrated by the end of the simulation at a strain of 27%. A strong correlation was found between the tendency for shear localization and retained shear-induced dilatation.

SECURITY CLASSIFICATION OF THIS PAGE

REPORT DOCUMENTATION PAGE

1a REPORT SECURITY CLASSIFICATION UNCLASSIFIED	1b RESTRICTIVE MARKINGS NONE
2a SECURITY CLASSIFICATION AUTHORITY	3 DISTRIBUTION / AVAILABILITY OF REPORT Approved for public release. Distribution unlimited.
2b DECLASSIFICATION / DOWNGRADING SCHEDULE	
4 PERFORMING ORGANIZATION REPORT NUMBER(S) Technical Report No. 6	5 MONITORING ORGANIZATION REPORT NUMBER(S)
6a NAME OF PERFORMING ORGANIZATION Massachusetts Institute of Technology 6b OFFICE SYMBOL (If applicable)	7a NAME OF MONITORING ORGANIZATION ONR
6c ADDRESS (City, State, and ZIP Code) 77 Massachusetts Avenue Cambridge, MA 02139	7b ADDRESS (City, State, and ZIP Code) 800 North Quincy Street Arlington, VA 22217
8a NAME OF FUNDING / SPONSORING ORGANIZATION DARPA 8b OFFICE SYMBOL (If applicable)	9 PROCUREMENT INSTRUMENT IDENTIFICATION NUMBER N00014-86-K-9768
8c ADDRESS (City, State, and ZIP Code) 1400 Wilson Boulevard Arlington, VA 22209	10 SOURCE OF FUNDING NUMBERS PROGRAM ELEMENT NO: R & T Code PROJECT NO: A400005 TASK NO: WORK UNIT ACCESSION NO:

11 TITLE (Include Security Classification)
SIMULATION OF PLASTIC DEFORMATION IN A TWO-DIMENSIONAL ATOMIC GLASS BY MOLECULAR DYNAMICS - IV

12 PERSONAL AUTHOR(S)
Deng, Derguo, Argon, Ali S., and Yip, Sidney

13a TYPE OF REPORT	13b TIME COVERED	14 DATE OF REPORT (Year, Month, Day)	15 PAGE COUNT
Journal paper	FROM 1/15/87 TO 8/15/88	1988 August 22	90

16 SUPPLEMENTARY NOTATION
Submitted to Acta Metallurgica.

17 COSATI CODES		
FIELD	GROUP	SUB-GROUP

18 SUBJECT TERMS (Continue on reverse if necessary and identify by block number)
Plastic flow simulation, glassy atomic media.

19 ABSTRACT (Continue on reverse if necessary and identify by block number)

Plastic deformation in a structurally well-relaxed two-dimensional atomic glass was simulated by a computer molecular dynamics approach. The simulation, which was carried through yielding and to substantial plastic strains, demonstrated that the principal mechanism of plastic strain production is by local partially dilatant shear transformations nucleated preferentially in the boundaries of liquid-like material separating the small quasi-ordered domains that form when the glass is well relaxed. Under imposed forward shear strain increments, local shear transformations in atomic clusters were found to be mostly in the same direction as the applied stress. There were, however, substantial levels of shear transformations in other random directions, including many opposed to the applied stress. In all instances, however, nucleation of shear transformations reduced the Gibbs free energy monotonically, which is governed largely by the locked-in excess enthalpies of the glassy state. At shear strains above 15%, localization of shear into bands was

(CONTINUES ON REVERSE SIDE)

20 DISTRIBUTION / AVAILABILITY OF ABSTRACT ☒ UNCLASSIFIED/UNLIMITED ☐ SAME AS RPT ☐ DTIC USERS	21 ABSTRACT SECURITY CLASSIFICATION UNCLASSIFIED
22a NAME OF RESPONSIBLE INDIVIDUAL A.S. Argon Ali S. Argon	22b TELEPHONE (Include Area Code) (617) 253-2217 22c OFFICE SYMBOL

DD FORM 1473, 84 MAR 83 APR edition may be used until exhausted. All other editions are obsolete

SECURITY CLASSIFICATION OF THIS PAGE

19. ABSTRACT (Con't.)

observed to begin. This steadily intensified and formed well-defined sharp shear bands into which all the shear strain became concentrated by the end of the simulation at a strain of 27%. A strong correlation was found between the tendency for shear localization and retained shear-induced dilatation.

I. INTRODUCTION

Amorphous solids make up a large group ranging from intrinsically brittle inorganic ones, such as the familiar oxide glasses, to glassy metallic alloys and polymers which exhibit extensive ductility in the unaged form and are embrittled when aged. While it is very difficult to initiate plastic flow in the intrinsically brittle family of glasses short of superposing very large components of pressure to suppress fracture, plastic flow to large strains is readily achievable in most unaged glassy metallic alloys and polymers.

The mechanisms of deformation in these materials have long been a source of controversy. While some investigators have sought to explain the plasticity of glasses by generalized dislocations [1,2], others have attributed it to the same cluster relaxations that give rise to viscous behavior [3-5]. Since drawing conclusions from observations of external features such as shear localization zones can be risky, and since the usual powerful methods of direct observations of defects based on diffraction contrast are inoperative, simulation of the deformation by various techniques have proved to be most fruitful. In one of the first of such attempts, Argon and coworkers [6,7] have performed shearing experiments on disordered Bragg bubble rafts as two-dimensional analogues of a real atomic glass, and analyzed the kinematics and energies of this deformation by means of an inter-bubble pair potential [8]. These analog simulations have demonstrated convincingly that the mechanism of plastic flow in simple disordered solids indeed involves very localized atomic cluster relaxations, and that dislocation glide, when present at all, plays only a minor role. These results

largely confirm the very limited amount of the earlier three-dimensional computer simulations [9]. Here, we present the results of a new two-dimensional computer simulation of the plastic shearing of the same two-component model amorphous solid discussed in the three accompanying communications, to be referred to here as I-III [10-12].

II. DETAILS OF SIMULATION

2.1 The Simulation Cell

A two-component material composed of equal numbers of Cu and Zr atoms was chosen for the simulation, since single component materials proved to crystallize too rapidly below the melting point [10]. Since visualization of the kinematic details of the local deformation processes were of primary interest, the simulation was carried out in two-dimensional cells subjected to periodic boundary conditions, so as to avoid spurious end effects. When a preliminary simulation cell containing 144 atoms on which detailed simulations of melting and quenching [10,11] had been carried out, gave indications of being too small for the shearing experiments, a larger 2-D simulation cell containing 780 atoms was chosen for most of the results to be presented here. This cell, which was nearly perfectly square, contained in its initial crystalline form 26 close-packed rows of 30 atoms. As we have discussed in connection with our simulations for melting, quenching, and structural relaxations, there are certain limitations of 2-D models when compared to 3-D models. Nevertheless, on the basis of our

findings, if 2-D cells containing 780 atoms are necessary to have minimal border effects and constraints, then a proper 3-D model should have over $2\text{x}10^4$ atoms. This would make the simulations themselves, as well as the graphical representation and analysis of the deformation exceedingly costly. We are of the opinion that the results of our 2-D simulation have captured the most important qualitative details, and have further given quantitative measures which compare quite well with experimental information on amorphous metallic alloys. Thus, the majority of the results we will present relate to the large 780 atom cell. We have, however, included a number of additional results derived from the smaller simulation cell of only 144 atoms.

The details of the $Cu - Zr$ pair potential, as well as the details of the procedures in carrying out the molecular dynamics simulation with it were presented in (I) [10], which also contains an appendix of nomenclature and normalization quantities. The most important of these normalization quantities are: for energies, $E_o(= 0.15eV)$, the binding energy for the $Cu - Cu$ pair potential; for lengths, $r_o(= 2.556\mathring{A})$, the critical atomic separation in the $Cu - Cu$ potential where the potential becomes zero; for 2-D stresses, $E_o/r_o^2(= 0.367N/m)$; for time $(r_o^2 m_o/E_o)^{1/2}$, the fundamental atomic period for $Cu(= 5.38\text{x}10^{-13}\text{sec})$, where $m_o = 10.63\text{x}10^{-23}\text{g}$ is the atomic mass of Cu, and for temperatures, $E_o/k(= 1740K)$. Since the simulation mats are two-dimensional, to obtain meaningful stresses in 3-D, the non-dimensional stress components and pressures must be multiplied by $E_o/r_o^3(= 1.44GPa)$. In the simulations, the fundamental

time steps were taken as 1/20 of the above atomic fluctuation period.

2.2 State Parameters and Inelastic Strains

Of fundamental interest in this simulation are the forms of inelastic strain production and the local environments in which increments of inelastic strain develop under externally-imposed conditions of stress or cell distortion. The most meaningful state parameters which describe the local conditions have been defined in (II) [11], in connection with the topological features of isothermal structural relaxations obtained in a preparatory simulation to the present one of plastic deformation. These local parameters of state are:

a. the volume per atom $\Omega(i)$ (the area of the Voronoi polygon constructed around each atom);

b. the free volume $s_f(i)$ of an atomic site (i.e., the excess volume per atom averaged over the atom and its immediate neighbors – over and above the average volume per atom in the entire simulation field);

c. the atomic level stress tensor $\sigma_{\alpha\beta}(i)$ (defined for each site by the procedure of Born and Huang [13]);

d. atomic level elastic constants $C_{\alpha\beta\gamma\delta}(i)$ (representing the local stiffnesses of each atomic site); and finally,

e. the net atomic site distortion parameter $w'(i)$ defined as the ratio of the perimeter of a Voronoi polygon of a site to the circumference of a circle having the same area. Of the atomic level stresses, two scalar invariants are of particular interest: the atomic site 2-D pressure, and the maximum (Mohr circle) shear stress.

When the simulation cell is deformed by imposed shear increments, the local internal increments of deformation are of interest. Most investigators who have performed similar simulations have provided only atomic displacement fields, which in our opinion, offer at best only a confusing image of the local processes, as they need a reference origin, and are not free of rigid body rotations, which are of no fundamental importance. For that reason, Argon and coworkers [6,7] have given the local deformations as atomic site shear strain increments and dilatations, which need no reference origin and are free of rigid body rotations. The tensor components of the strain increments have been defined as weighted area integrals of the local deformation gradients as follows:

$$\Delta\epsilon_{\alpha\beta}(i,\Delta t) = \frac{1}{2s_i} \int_{s_i} \left(\frac{\partial \Delta u_\alpha}{\partial \beta} + \frac{\partial \Delta u_\beta}{\partial \alpha} \right) ds \ , \tag{1}$$

$$= \frac{1}{2s_i} \sum_{j=1}^{n} \left[\frac{\Delta u_\alpha(j) - \Delta u_\alpha(i)}{\Delta \beta} + \frac{\Delta u_\beta(j) - \Delta u_\beta(i)}{\Delta \alpha} \right] \Delta s_j \ , \tag{1a}$$

where $\Delta u_\alpha(j)$ and $\Delta u_\alpha(i)$ are the displacement increments for atoms j and i in the α direction occurring in the time increment between t and $t + \Delta t$, i.e., between the start and finish of an imposed strain increment on the simulation cell; $\Delta\alpha$ and $\Delta\beta$ are initial relative separations of atoms j and i in the α and β directions at time t. The term Δs_j represents the triangular area of the Voronoi polygon (VP) of atom i that views the neighboring atom j; s_i is the total area of the VP of atom i, and the sum on j is over all neighbors of i that enter into to description of the VP of the atom i. These definitions of strain increments can also be transformed by the divergence theorem into contour integrals around the periphery ℓ_i of the VP of each atom i, when they become (in x, y coordinates):

$$\Delta\epsilon_{xy}(i, \Delta t) = \frac{1}{2s_i}\left(-\oint_{\ell_i} \Delta u_x \; dx + \oint_{\ell_i} \Delta u_y \; dy\right) \quad , \tag{2}$$

$$= \frac{1}{2s_i} \sum_{j=1}^{n}\left[-\frac{(\Delta u_x(j) + \Delta u_x(i))}{2}\Delta x_j + \frac{(\Delta u_y(j) + \Delta u_y(i))}{2} \; \Delta y_j\right] \quad , \tag{2a}$$

where $\Delta u_x(j)$ and $\Delta u_x(i)$ again represent the displacement increments for atoms j and i in the x direction occurring in the time increment between t and $t + \Delta t$ between the start and finish of an imposed strain increment on the simulation

cell, and Δx_j represents the component in the x direction of the edge of the VP viewing the neighboring atom j of the central atom i, and again, the sum on j is taken over all neighbors of i that enter into the description of the VP of the atom i.

As with the local atomic level stresses, two scalar invariants of the local strain increments are of special interest, the local dilatation $\Delta\epsilon(i)$, and the local increment of the (Mohr circle) maximum shear strain $\Delta\gamma_{max}(i)$, which are defined as:

$$\Delta\epsilon(i) = \Delta\epsilon_{xx}(i) + \Delta\epsilon_{yy}(i) \quad , \tag{3}$$

$$\Delta\gamma_{max}(i) = 2\sqrt{(\Delta\epsilon_{xx}(i) - \Delta\epsilon_{yy}(i))^2 + (\Delta\epsilon_{xy}(i))^2} \quad . \tag{4}$$

In what follows, we will present our results primarily as atomic site information of the current state and increment of inelastic strain.

2.3 The Shearing Simulation

The shearing simulations were carried out on two different sizes of periodic cells. In both instances, the material was a 2-D mat composed of equal numbers

of Cu and Zr atoms, bound together by three different pair potentials, to take into account the $Cu-Cu$, $Zr-Zr$, and $Cu-Zr$ interactions. In both cases, the initial state of the material was a hexagonal 2-D crystal solid solution, in which the individual Cu and Zr atoms were placed randomly. Both mats were melted in the computer and quenched in steps, at an average rate of about $2\text{x}10^{9}\text{Ksec}^{-1}$, to a low temperature, followed by a period of structural relaxation of the order of 4000 time steps. The details of the potentials, the melting and quenching simulations, and the descriptions of the molten state, as well as the low temperature quenched states, were described in detail in the accompanying communications (I and II) [10,11]. The small simulation cell, which contained 144 atoms in 12 rows of 12 close-packed atoms, was rectangular in shape, with the edge parallel to the x axis being 15% longer than that parallel to the y axis. This cell, on which nearly all the earlier melting, quenching, and structural relaxations were performed, which have been reported in (I and II), proved to give asymmetrical results upon being subjected to simple shear in the x and the y directions. To rectify this asymmetry and also to incorporate a larger field to sample more configurations, the second simulation cell was selected to be square in shape, with 30 vertical stacks of close-packed rows containing 26 atoms each, and thus, consisting of 780 atoms on the whole. To check the thermo-physical properties of this material, and relate them to those of the smaller mat, the simulation for the large mat was also started with a melting and quenching sequence identical to those for the smaller mat. The melting temperature and the glass transition temperature for the larger mat were identical to those of the smaller mat. The only difference between the two mats was a constant coefficient

of expansion for the larger mat in the crystalline region prior to melting, rather than the somewhat more curved expansion curve that had been obtained for the small mat. The areal expansion of the large system with changing temperature is shown in Fig. 1. Figures 2a and 2b show the structure of the large mat at the melting point of $T^* = 0.25$ and at $T^* = 10^{-3}$ after 4000 time steps (200 fluctuation periods) of structural relaxation, respectively. As can be seen, the structure of the relaxed glass is composed of quasi-ordered domains, separated by boundaries of liquid-like material composed of ordered sequences of 5 and 7 sided polygons, which in pairs, represent edge dislocation cores. Figure 3 shows the RDF of the relaxed glass in the large mat before the shearing simulation at $T^* = 10^{-3}$. This compares well with the RDF of the relaxed smaller mat, shown in Fig. 11d of (I) [10].

In the shearing simulation, the external shear strain increments were kept quite small at $5\text{x}10^{-4}$, so as to be able to resolve elementary processes in the interior. These shear increments are much smaller than those imposed by Srolovitz et al. [9], or by Maeda and Takeuchi [14]. The shearing was done deliberately at constant volume to stabilize the dilatancy effects producing early shear localization. To monitor the expected effects of shear localization, however, the change in external pressure in response to the imposed shear was calculated for each increment of shear strain. Since the starting state of the material for the shearing simulation was obtained by quenching and relaxing a previously melted mat, all at an imposed external pressure of $p^* = 1.0$, the shearing simulation at constant volume also started with this superimposed pressure.

The increments of shear strain were applied by shearing all atoms into new positions by an affine simple shear transformation in the positive y direction. To test for possible asymmetries in the behavior of the mat, shearing was also done parallel to the x direction, and resulted in very similar results, without any sign of asymmetry. Whether the asymmetry in the behavior of the small mat resulted from its small size or its rectangular shape, was not explored further. In any event, the majority of the results to be presented here are related to the large mats, which had symmetrical and isotropic behavior. Upon the application of a shear strain increment, the atom positions were relaxed by the MD procedures. The time dependent relaxations of the average enthalpy per atom after an affine shear strain increment are given in Fig. 4, which shows that the most unnatural rise in enthalpy due to the imposed affine re-positioning of the atoms is eliminated after about 190 time steps, or about 10 fluctuation periods. Relaxations continue more slowly after this time, and would eventually eliminate any metastable states associated with production of dilatancy and related effects that were of interest. Therefore, the relaxations were stopped after 190 time steps, followed by a new increment of shear strain, and so on. Parenthetically, such rates of shear amount to $10^8 sec^{-1}$ in real time. The shear induced intensive properties associated with each atom were calculated after each shear increment. Both the incremental changes in the intensive parameters, and the accumulated totals were obtained at certain strain levels in the stress strain curve, and will be presented in detail in what follows.

III. RESULTS

9.1 Elastic Bulk Properties

The elastic properties of the small mat in bulk response was investigated by changing the cell area systematically in small increments in both directions, to determine the pressure response. The resulting volume average pressure-volume curve is shown in Fig. 5a, from which the small strain, two-dimensional bulk modulus K_{2D} under a pressure of 1.0 can be determined readily around this initial pressure, i.e., at $v/v_o = 1.0$, which was 48 in dimensionless stress. This will be compared below with the apparent shear modulus obtained from a shear stress, shear strain simulation curve. The atomic displacements and their character that accompanied this volumetric deformation were not studied. It is expected that some inelastic volumetric relaxation had accompanied this deformation. Weaire at al. [15], found in a similar 3-D study, that the inelastic relaxations in volumetric deformation were much less extensive than the corresponding shear relaxations accompanying an apparent elastic response. We expect this to be the case here also. As an added feature to this volumetric response, the shear stress changes that result on the borders of the mat were also monitored, and are shown in Fig. 5b. As expected, there were no shear tractions evoked by the volumetric strains – beyond random fluctuations.

From the curvature of the pressure-volume curve of Fig. 5a, the pressure dependence of the two-dimensional bulk modulus can be determined readily,

and is shown in Fig. 6. It is found to be quite constant over a wide range at a value of:

$$\frac{dK}{dp} = 19 \qquad (5) \ .$$

Because of the non-dimensional nature of the information, we expect that the value given in Eqn. (5) also represents the pressure dependence of the three-dimensional bulk modulus.

By extrapolation of the line in Fig. 6 to zero bulk modulus, we find that the bi-axial cohesive strength σ_i of the mat is 1.55 in dimensionless stress units. The ratio of this to the 2-D bulk modulus of 18.8 at zero pressure gives a value of 8.2×10^{-2}, which we find quite reasonable. Extrapolation of the curve in Fig. 5a to zero slope gives the critical areal strain for 2-D decohesion as 0.175.

3.2 Shear Response

The elasto-plastic shear response of the large mat up to a total shear strain of 0.27, is shown in Fig. 7. A clear initial elastic region is visible with a gradual elasto-plastic transition that is complete at a shear strain of around 0.08, where the boundary shear tractions level off at a value slightly above 1.0 in dimensionless stress units. There are considerable variations in the shear resistance between increasing increments of shear strain. This is to be expected

from the relatively small nature of the simulation cell, which even with 780 atoms contains only quite finite numbers of strain producing configurations. The apparent 2-D shear modulus μ_{2D} obtained from the average slope of the initial linear region was found to be 16 in dimensionless stress units under a pressure of $p^* = 1.0$. From this shear modulus and the 2-D bulk modulus presented in Section 3.1 above, the fundamental elastic properties of the three-dimensional reference material under a pressure of $p^* = 1.0$ can be determined through some well-known relations:

$$K_{2D} = \frac{s_{11}}{2\left(s_{11}^2 + s_{11}s_{12} - 2s_{12}^2\right)} \quad , \tag{6a}$$

$$K_{3D} = \frac{1}{3\left(s_{11} + 2s_{12}\right)} \quad , \tag{6b}$$

$$\mu_{2D} = \mu_{3D} = \frac{1}{2\left(s_{11} - s_{12}\right)} = \frac{1}{s_{44}} \quad , \tag{6c}$$

$$E = \frac{1}{s_{11}} \quad , \tag{6d}$$

$$\nu = \frac{-s_{12}}{s_{11}} \quad , \tag{6e}$$

where K_{3D} is the 3-D bulk modulus, E the 3-D Young's modulus, ν the Poison's ratio, s_{11} is the tensile compliance, s_{12} the transverse compliance, s_{44} the shear compliance, and $\mu_{3D} = \mu_{2D}$ is the shear modulus of the amorphous alloy. In the determination of K_{2D}, a three-dimensional solid was considered stretched in only two dimensions under a constraint of no deformation in the third direction. From the simulation results of $\mu^* = 16$ and $K^*_{2D} = 48$, the following values were determined from the relations given above: $s^*_{11} = 2.35\text{x}10^{-2}$, $-s^*_{12} = 7.80\text{x}10^{-3}$ in reciprocal dimensionless stress units, $K^*_{3D} = 42.2$, $E^* = 42.6$ in dimensionless stress units, and $\nu = 0.332$. The absolute values of the 3-D moduli are lower by about 25% than the values reported by Davis [16] for amorphous metals. The calculated Poisson's ratio is quite close to the values reported for close packed metals, but considerably lower than the very high value of 0.41 reported by Davis [16]. We take these results as quite representative, considering that 2-D solids usually entrap higher levels of free volume in the amorphous state, and should therefore, have lower moduli.

We note that the ratio of the yield stress in shear to the shear modulus is $6.25\text{x}10^{-2}$. This is about a factor of 2 higher than the values exhibited by

amorphous metals, back extrapolated to $0^{o}K$ [17,18], but less than 1/3 of the value obtained in the 3-D computer simulation of Srolovitz et al. [9]. The latter simulation was also performed by shearing at constant volume, but was performed on a simulation cell so small that it was likely to be too confined to represent a realistic sampling of the possible shearing configurations. Figure 7 shows a dip in the plastic resistance at a total shear strain of 0.15. Although the exact cause of this dip is uncertain, the behavior could be associated with a large increase in the concentration of liquid-like material in the mat observed at this same shear strain, which we will discuss in Section IV below. If this is indeed the case, the dip should be attributed to a size effect in the simulation cell. Outside of this long wave length variation, the flow stress remains roughly constant up to the largest shear strain of 0.27. Thus, the simulation material acts as an ideally plastic solid, with no strain hardening.

Simulations of amorphous media by others [15] have shown that when compared with their crystalline counterparts, the elastic moduli of the amorphous materials are lower, but that while this reduction is only a few percent for the bulk modulus, it is 15-20% for the shear modulus. This difference has been explained by a larger concentration of anelastic non-affine changes in the apparent elastic range in shear processes, than in bulk expansion. To test this possibility, as well as to probe the inhomogeneity of the local processes, the shearing direction was reversed after a forward strain of 0.025, as well as after 0.075 and 0.125, until in each case unrestrained plastic deformation in the reverse direction occurred. This is seen in Fig. 8, which shows that the unloading in the apparent elastic range (the upright crosses) after a forward strain of 0.025 does

not follow the loading curve, but rather shows a substantial anelastic hyteresis behavior. The total inelastic residual strain, when the reversed shear stress is zero, is around 0.01, or quite close to 40% of the forward strain. The reverse loading behavior at the border of the elasto-plastic transition at 0.075 strain (the inclined crosses) and in the unrestricted plastic flow region at 0.125 strain (the upright triangles) show very pronounced Bauschinger effects. The total inelastic residual strain upon complete unloading of the stress was 0.04 and 0.09, respectively, for the two reverse loading paths after 0.075 and 0.125 forward strain. These residual strain magnitudes and inspection of the unloading curves show directly that the initial unloading slopes are considerably higher than the loading slope. Direct determination of these initial unloading shear moduli from Fig. 8 gave a value of 39 in dimensionless stress units. In an uncomplicated elastic-plastic solid, with no hardening and no rate effect, such an apparent increase in the unloading modulus would be difficult to explain. In our simulation material, however, where considerable anelastic behavior is exhibited, such increases in the unloading modulus signify continued forward deformation under stress during the early portion of the unloading. Thus, more rapid unloading should result in a lower unloading modulus, and vice-versa for a slower rate of unloading.

3.3 Pressure Response to Shearing

It is well known that plastic shearing of a strúcturally relaxed disordered material increases the disorder due to an intrinsic dilatancy effect.

Such deformation induced dilatations have been measured by Deng and Lu [19], and Argon et al. [20], in amorphous $Pd_{77.5}\ Cu_6\ Si_{16.5}$ alloy. Since our shear simulations were carried out at constant volume, the developing dilatancy was expected to increase the pressure on the simulation cell. This was found to be the case in both the small simulation cell as well as in the large one. Figure 9 shows the developing pressure upon shearing in the large system. In the beginning, there is a sudden and unexplained rise in the pressure, which decays slightly in the strain range of $0 - 2.5\text{x}10^{-2}$, but then rises monotonically to an asymptotic level of 1.6 in dimensionless stress units at a strain of 0.13: beyond this, it remains roughly constant. The rising portion of the curve between 0.025 and 0.13, when extrapolated backwards toward the ordinate line, gives an intersection roughly at a pressure of 1.0, which was the pressure under which the earlier structural relaxation was carried out. The reason for the initial step rise in the response is unclear. After about 0.13 of strain, conditions remain unchanging. As we will see below, this coincides with the beginning of perceptible shear localization. It is expected that shear localization due to dilatancy should begin very early in the deformation process, but that the conditions of deformation at constant volume have been responsible for its delay to a strain as large as 0.13.

To explore the changes in the shear induced pressure response, the pressure on the system during the two reverse loading histories, starting at $\gamma = 0.075$ and 0.125, was also monitored and is shown in Fig. 10. Reversal of deformation results in a rapid and dramatic decrease in the previously built-up pressure, reaching a minimum of $p^* = 1.0$ at the point where the reverse stress strain

curve crosses through the point of zero shear stress. Clearly, the decrease in the pressure must be due to reversals of many of the shear transformations just accomplished prior to the reversal of deformation. Such transformations are expected to have nearly identical environments of residual back stress and associated pressure, which could be systematically reversed as these transformations are reversed. Once the supply of these most recent transformations is exhausted in reverse deformation, the early history is wiped out, and new reverse transformations have to be initiated in fertile but neutral material. Finally, from the shear induced increase in pressure of $\Delta p = 0.6$ between 0-0.13 strain, and the 2-D bulk modulus of 59 at the final pressure of 1.6, where steady conditions of flow are reached, we calculate an overall change of dilatancy effect of $(\Delta v/v)/\Delta\gamma^p = 0.151$ for a total plastic strain increment of $6.75\text{x}10^{-2}$ between 0-0.13 total strain.

3.4 Change in Enthalpy and Structure due to Plastic Shearing

The dilatancy of the shearing process serves to make the material more amorphous and raises its excess enthalpy. At the very low temperature, where the simulation was performed, the major contribution to the enthalpy of the system is through its change of potential energy (see Appendix I). Figures 11a and 11b show the change in potential energy with forward shear and the two special paths of reverse shear, respectively. The potential energy changes are parallel to the changes in deformation induced pressure resulting from the dilatancy, which itself is a direct cause of the rise in enthalpy.

The corresponding changes in the structure due to dilatancy induced amorphization are also apparent in the RDFs. Figure 12 shows the RDF of the material at a strain of 0.10. Comparison of this with the RDF in Fig. 3 shows a very clear broadening of the distribution with decreases in the peak heights and filling-in of the regions between the peaks. This change in the RDFs due to re-amorphization proceeds most rapidly in the very early straining range between 0 - 0.08, where fully established plastic flow conditions are achieved, but continues more slowly up to 0.13, where the rise in shear induced pressure ceases. After about 0.10 (the state in Fig. 12), the further changes in the RDF with shearing are less dramatic than in the early phases. The observed amorphization is a consequence of plastic shearing, even in the apparent elastic range, where as we will see below, inelastic transformations occur with sufficient frequency.

3.5 The Topological Features of Local Plastic Flow

3.5.1 Plastic flow at yield. To establish the nature of plastic flow in the simulation, we present first the distribution of local shear transformations and describe the environments in which they occur for a small plastic strain increment of $\Delta\gamma^p = 5\text{x}10^{-4}$ near the macroscopic yield region of the elastic to plastic transition, at a total strain of $\gamma = 0.05$.

Figure 13 shows the incremental displacement field of the atoms in units of the fundamental length r_o, during the plastic increment. Each displacement vector emanates from the atom with which it is associated. Such a displacement field, presented by most investigators in the past, as the only feature of the plastic deformation is too confusing to provide much enlightenment. Nevertheless, it is possible to outline in it regions where the most intense activity is concentrated, such as the four regions that have been delineated by closed contours. They resemble to some extent the zones of concentrated "C" and diffuse "D" shear transformations identified by Argon and Kuo [6] in sheared Bragg soap bubble rafts. Here, we will not pursue details of displacement fields further, but rather concentrate our attention on the field of local strain spikes introduced first also by Argon and Kuo [6]. Thus, Fig. 14a shows the incremental maximum shear strain spikes (regardless of their principal axes) that have resulted during the specific macroscopic plastic strain increment under consideration. The accompanying local dilatation spikes (upright triangles represent positive quantities) are shown in Fig. 14b. Since the simulation has been performed under constant volume conditions, the volume average sum over all the dilatation spikes should give zero. Clearly, many dilatancy events have been either suppressed or perhaps even reversed by this condition – or in the least have affected their surroundings somewhat by pressurizing the background.

Inspection of Fig. 14a shows that the local shear strain spikes are quite large, with many of them being in the range of 0.05-0.10, and some being even somewhat larger. This occurs during an external total strain increment of only $5\text{x}10^{-4}$. Thus, clearly, the local plasticity is in the form of shear transforma-

tions, with transformation shear strains of the order of 0.05-0.10 in local volume elements. This is quite similar to the kinematics of plastic flow studied by Argon and Shi [7] in the Bragg soap bubble rafts, where transformation shear strains of these magnitudes were also observed.

A point of primary interest in this simulation is the description of the most relevant state parameter of the local environment, in which the local shear spikes develop. Four primary candidates that must be considered are shown in Figs. 15a-15d. They are:

a. the local atomic level maximum shear stress (regardless of orientation of principal axes);

b. the atomic level pressure and negative pressure (upright triangles represent pressure);

c. the local free volume; and

d. the local atomic site distortion parameter;

all evaluated at the beginning of the specific small plastic strain increment, which is the subject of discussion.

Comparison of Figs. 14a and 14b shows a reasonable visual correlation between the local dilatations and the local shear strain spikes everywhere in the field, but especially in the upper right quadrant and along the diagonal zone radiating from the center of the figure into the upper left quadrant. Correlation of the shear spike distribution with the distributions of the atomic level maximum shear stress and atomic level pressure, shown in Figs. 15a and 15b,

is weak at best. The best evidence of any such correlation is in the center of the cell, in small portions of the lower left-hand quadrant and lower right-hand corner of the lower right-hand quadrant for the maximum shear stress. For the pressure, the correlation is roughly at the same places, but even weaker. On the other hand, the correlation between the sites of the maximum shear strain and both the free volume (fig. 15c) and the atomic site distortion parameter (Fig. 15d) is quite striking. The latter two are, of course, specific quantitative characterizations of the boundaries between the quasi-ordered domains, where the liquid-like material concentrates, as can be seen by comparing Figs. 15c and 15d with Fig. 2b. That this is bound to be the case, must be clear from the fact that in the liquid-like material, there is a concentration of excess free volume and the local distortion. This has produced a significant reduction of cohesive interaction, as we have discussed in (I) and (II) in detail [10,11], and as can be deduced also from the discussion in Section 3.1 above.

3.5.2 Character of shear transformations. Since the plastic shear events are enforced by the imposed $\Delta\gamma_{zy}$ shear (or alternatively by the applied shear stress σ_{zy}), it is of interest how well the local shear spikes are polarized by these "driving forces". To probe this, only the $x-y$ components of the shear spikes were determined, and their magnitudes are plotted in Fig. 16. A cursory check of the integrated magnitudes of these shear strain spikes has shown that this total integral over the field exceeds considerably the applied shear increment of $5\text{x}10^{-4}$. This observation disclosed that a significant fraction of the total shear events shown in Fig. 16 are actually of a negative sign, and occur against the applied

stress. Figure 17 shows the distribution of both the positive and negative shear spikes during the specific plastic strain increment. This starting behavior of reverse local shear against the applied shear stress is readily explained when it is recognized that the root mean square level of excess enthalpy associated with the structural disorder is many times larger than the work done by the applied stresses interacting with the local strain increments. Thus, as primary shear transformations occur in and around the liquid-like regions, they momentarily destroy local mechanical equilibrium and permit some surrounding material to lower its Gibbs free energy, even at the expense of doing work against the applied stress. This fact was confirmed by studying the Gibbs free energy change for a number of local cluster systems as a function of strain in which shear transformations had been observed, regardless of sign. In all instances, the Gibbs free energy was found to decrease monotonically (see Appendix I), as a function of increasing average strain. Two typical cases are shown in Figs. 18a and 18b. Of these, Fig. 18a pertains to a case of positive local shear strain, while 18b pertains to a case of negative local shear strain. These figures also show that the monotonic decline of the free energy is interrupted at many places by energy barriers of varying height. These are interpreted as barriers that can be overcome by thermal activation under a constant applied stress at higher temperature. Accordingly, the frequency distribution of these barrier heights was determined over the history paths of six separate clusters as an indication of the distributed nature of the shear relaxation processes. This distribution is shown in Fig. 19. It demonstrates that while the majority of the energy barriers are less than E_o (i.e., 0.15 eV), some are nearly a factor of 10 larger. The informa-

tion derived from these observations, however, is too incomplete for purposes of quantitative comparisons with experimental distributions of the type studied in detail by Deng and Argon by internal friction measurements [21,22].

Examination of Fig. 17 also shows that once the forward and reverse shear processes are separated, a significant amount of clustering of shear processes of either type becomes more apparent. Among these clusters, those that are of elongated and concentrated shear type, as classified by Argon and Kuo [6], immediately stand out. The diffuse shear transformations, as usual, are more difficult to identify. Part of this difficulty is associated with the lack of time resolution in the chronology of appearance of individual processes. Even in the span of a very small plastic strain increment, such as the one on which the information in Figs. 14-17 is based, many transformation events, actually separated in time, have become superimposed.

The proximity of the clusters producing positive and negative shear to each other also attests to a cause-effect relationship between the two. The change in local atomic configurations during the development of a forward shear cluster upsets mechanical equilibrium in the immediate surrounding regions, and can trigger a reverse shear-producing cluster if the initial misfit incorporated in that region is conducive for such a reverse transformation.

A similar form of clustering is also perceivable in the distribution of the dilatation spikes, shown in Fig. 14b. In many regions where upright triangles are clustered indicating dilatation increments, the immediate local surroundings show rings of downright triangles indicating inelastic local compaction. Both of these changes correlate reasonably well in spatial distribution with the shear

processes, as already pointed out above.

Examination of the distributions of local coupled shear and dilatational transformations in different regions of the stress strain curve indicated that regions in which transformations were found in earlier stages of straining could transform again, later. Since in the vast majority of cases the shear transformations occurred in and around the boundaries of liquid-like material separating quasi-ordered domains; this repetition, in time, of local shear activity in the fertile boundary regions, attests to the true liquid-like nature of this material. Since these boundaries were not planar but intricately tortuous, increasing strain must shift them around, so as not to build up large plastic misfit stresses in the quasi-ordered domains. That this is indeed the case can be seen from the set of frames shown in Figs. 24a-24d.

3.5.3 The elastic-to-plastic transition. In Section 3.2, it was demonstrated by means of reverse loading within the apparent elastic range, that inelastic non-affine processes must be occurring even in this range of response of the material. That this is indeed so, is shown in Figs. 20a-20c, which shows the total accumulated γ_{xy} strain in the apparent elastic range at total average strains of 0.0125, 0.025, and finally at 0.05, where the most rapid transition to fully developed plastic flow begins. Examination of these three plots shows that inelastic strains in this range do not spring-up as shear transformations with the same full strength as they have during fully developed plastic flow. They rather grow gradually and incrementally in fertile regions that lie in or near to the liquid-like material. Thus, they are more of an anelastic nature, permitting

them to return to nearly the undistorted state of the material when the stress is removed – albeit accompanied by a hysteresis effect.

3.5.4 Shear strain localization. The dilatant nature of plastic flow in ductile amorphous media has been proposed to be the source of strong shear localization in these materials at low temperatures and high strain rates [4,5,20,23], where the shear induced free volume or newly formed liquid-like regions do not decay fast enough by thermally controlled structural relaxations. This should be particularly the case at the low temperature of the present simulation. These regions then catalyze further shear transformations and progressively localize the deformation into intense planar shear zones [5,23]. This phenomenon has been observed directly in the simulation cell. Figures 21a-21d show a sequence of cumulative shear activity in the strain range of 0.05-0.2. The localization of shear into planar zones in the simulation cell is apparent. To establish the connection of this localization to dilatancy, both the incremental changes in local volume (Figs. 22a-22d), as well as the total accumulated dilatation (Figs. 23a-23d) was determined for these four states of total strain. It needs to be kept in mind that the simulation was carried out under conditions of constant volume. Therefore, the total integrated volume changes must be zero for all cases, and the total dilatation must be the same as that in the initial state of the simulation. Thus, the intrinsic dilatancy of the flow, which clearly manifests itself in the shear induced pressure rise, shown in Fig. 9, must produce local inelastic dilatation spikes in regions of flow concentration as well as some spikes of material compaction in the immediate neighborhood. Clearly, in this process, the inelastic dilatations

must dominate, since they elastically pressurize the entire simulation cell. The sequence of Figs. 22a-22d show that incremental dilatancy activity does indeed fall into the zones of the apparent shear localization. The correlation is much more striking when viewed as the total accumulated dilatations, as shown in Figs. 23a-23d, where the correlation of the localized accumulated dilatations with the localized shears, shown in Figs. 21a-21d, is clear.

IV. DISCUSSION

As stated in Section I above, the description of the mechanism of plastic flow in amorphous media has created much controversy. Gilman [1], Li [2], and others [24,25] have drawn specific analogies between the plastic flow mechanisms in nearly perfect crystals, where long range mobility of crystal dislocations produces strain, and the plastic flow in amorphous metals, where shear localization is frequently observed at low temperatures and high strain rates [4,20,26]. Two compelling points in support for this view are the observed intense shear localization process, as already mentioned, and an observed second order kinetics in the thermal recovery behavior of deformed samples [27], not to mention the great attraction to immediately capitalize on many other explanations of crystal plasticity for allied phenomena observed in amorphous metals. Many adherents of this point of view have extended the anology also to glassy amorphous polymers, even though there the chain molecules would introduce important constraints to any concentrated shear process. Since there are important differences even in the phenomenology of the deformation of polymeric materials, we will not pursue

their discussion here further either for or against the above point of view.

A separate compelling reason for taking a dislocation point of view for the behavior of amorphous atomic solids, is the many thought provoking theoretical studies of a topological nature of transforming a crystalline solid into an amorphous one by progressively dislocating it [28,29]. A further stimulus in this direction comes from equally interesting studies on the melting of crystalline solids by introducing increments of disorder through dislocations, and demonstrating that this process can give rise to sharp melting behavior (for a general review of the early work, see Nabarro [30]). When carried out with care [31,32], both the latter and the former theoretical studies do indeed lead to relaxed structures that exhibit most of the quantitative signatures of the glassy state. On the basis of this, it could then be argued that the dislocations that have led to the end state might have vestigial properties that can be mobilized for the processes of plastic deformation – in spite of the fact that the amorphous condition can be reached also by melting and severe radiation damage [33]. Nevertheless, the attraction of this indirect reasoning should be clear in the light of what we have presented in this and two of the associated communications (I) and (II) [10,11]. In these studies, we see, however, that the role of the dislocations and their vestigial properties are not to provide mobile configurations, but to introduce fertile matter that makes possible plasticity by shear transformations, which have no mobile properties, but are initiation controlled.

The alternative mechanism to explain plastic flow in amorphous atomic media is based on shear transformations in local small atom clusters proposed first by Orowan [3] to explain viscous deformation. This was later generalized

by Argon and coworkers [5-7,17] to explain most observed inelastic phenomena in atomic glasses, including the rate process of deformation, the temperature dependence of the flow stress over its entire range from 0^oK to T_g, and the distributed nature of the rate controlling process. Separately, Spaepen and coworkers [4,34] have developed a point of view of shear relaxations in a region of the volume where enhanced mobility of atoms should be preferred because of the lowered level of cohesive interactions. This mechanism of plasticity by local shear transformations has found support from many other investigations, including those based on computer simulations [9,35]. These latter investigations and the simulations based on the disordered Bragg bubble model [6,7] have provided important information on the particular fertile neighborhoods, in which shear transformations develop.

Thus, our simulations on melting, structural relaxations, and on plastic flow, presented in (I), (II) [10,11], and in this communication, have given a certain unification to many of these diverse points of view. The simulations on melting and structural relaxations have demonstrated that the disorder in the amorphous material can be divided into quasi-ordered regions of very small dimensions of 3-10 atoms across and internally disordered boundaries, surrounding these quasi-ordered regions. These boundaries, which percolate through the entire structure, exhibit topological signatures of dislocation cores that are apparent in the form of ordered sequences of 5 and 7 sided polygons. Here, contact is made with the dislocation theories of melting and amorphization [28,29,31,32], and other analog simulations using vibratory agitation of Bragg bubble rafts [36]. The present simulation on plastic flow on the other hand, has reinforced rather strongly

the points of view of deformation by nucleation of shear transformations in fertile regions, which have turned out to be along the percolating boundaries of disordered material composed of dislocation cores. Here, contact has been made with theoretical studies on fluidity in melts and subcooled melts, attributing the fluidity to liquid-like material percolating through the structure [37,38].

We recognize that the simulations presented here and in the associated studies of (I) and (II) are two-dimensional, and that three-dimensional material will have another degree of freedom in accomplishing the topologically complex re-distribution of structural disorder and re-positioning of atoms in shear transformations. We maintain, however, that our simulations have captured the qualitative essence of these complex processes, which differ in three-dimensional matter only quantitatively. On the other hand, the powerful capability of visualization of processes in a plane, have been in our view, of vital importance.

Since in our simulation mats of well-relaxed glasses small quasi-ordered regions exist, the lack of a contribution to the overall strain by dislocation glide is surprising. Actually, some evidence for such isolated glide events have also been found. In addition to the short range glide motion under the mutual interaction of two 60° dislocations during structural relaxation that has already been pointed out in (II) [11] (see Figs. 3a-3e in (II), a rare instance of stress initiated glide is shown in the deformation sequence of Figs. 24a-24d, in which the stages in the mat are seen between a total shear strain of 0.05 to 0.20. In Fig. 24a, a closely spaced dipole of dislocations is seen in the region marked as A. In the successive frames, the dipole is separated, and the two dislocations are driven apart. In Fig. 24b, the positions of the dislocations are marked with

arrows. In Fig. 24c, the dislocation on the right has already been incorporated into boundary, while the one on the left has entered the simulation cell on the other side, and is shown with an arrow. In Fig. 24d, this dislocation seemed to have been trapped by the boundary which has reached it. The shear strain contributed to the total strain in the simulation cell can readily be estimated as bx/A, where x is the total distance of separation of the dislocations, i.e., about 20 Voronoi polygons, b is the Burgers vector, and A the area of the mat, i.e., 780 Voronoi polygons. This gives a strain contribution of $20/780 = 0.0256$, which makes up about 11% of the total inelastic strain in the simulation, and thus, is not a negligible amount. There were, however, no other unambiguous glide events that could be found. There are two reasons why such events are not more numerous. First, the dislocation glide appears to be subject to a significant lattice drag, indicated by the many metastable configurations of two adjoining polygons of 5 sides, and the near impossibility of operating dislocation sources at the lower stress levels within the confines of the very small quasi-ordered regions. Thus, the shear transformations dominate the deformation even though they have no mobile character, but have the overwhelming advantage of a large volume fraction of fertile material, where they can be initiated.

Figures 24a-24d also show that as the deformation proceeds, the liquid-like material itself deforms and re-constitutes itself in a non-affine manner. In fact, the overall fraction of the liquid-like material itself varies in a fluctuating way, as the shearing continues. This is shown in Fig. 25, where the total numbers of non-hexagonal Voronoi polygons are plotted as a function of strain. The figure shows that the initial high concentration of this fertile material is depleted with

shear in the apparent elastic range of deformation. Further, shearing produces relatively large amplitude variations due to the shear induced dilatations and compactions. Around a strain of 0.15, a significant increase in the fraction of this material takes place. This coincides with the dip in the flow stress, shown in Fig. 7, and is most likely the explanation for it.

ACKNOWLEDGEMENT

This research has been supported by several sources. The early phases of the simulation on the smaller periodic cells were supported by the NSF through Grant No. 8517224-DMR, while the latter stages of the simulation on the large simulation cells requiring greatly increased levels of computations, became possible through the support of the Advanced Research Projects Agency under Contract N00014-86-K-0768. Additional salary support for DD was provided by the Allied Corporation through a fellowship for which we are grateful to Dr. Lance Davis. We also acknowledge a number of useful discussions with Professor D.M. Parks on presentation of strain spikes.

REFERENCES

1. J.J. Gilman, in "Dislocation Dynamics", edited by A.R. Rosenfield et al. (McGraw-Hill: New York), p. 3 (1968).

2. J.C.M. Li, in "Frontiers in Materials Science", edited by L.E. Murr and C. Stein (Marcel Dekker: New York), p. 527 (1976).

3. E. Orowan, in "Proc. First U.S. Nat. Congr. Appl. Mech." (ASME: New York), p. 453 (1951).

4. F. Spaepen, *Acta Metall.*, *25*, 407 (1977).

5. A.S. Argon, *Acta Metall.*, *27*, 47 (1979).

6 A.S. Argon and H.Y. Kuo, *Mater. Sci. Engrg.*, *39*, 110 (1979).

7. A.S. Argon and L.T. Shi, *Phil. Mag.*, *A46*, 275 (1982).

8. L.T. Shi and A.S. Argon, *Phil. Mag.*, *A46*, 255 (1982).

9. D. Srolovitz, V. Vitek, and T. Egami, *Acta Metall.*, *31*, 335 (1983).

10. D. Deng, A.S. Argon, and S. Yip: (I), submitted to *Acta Metall.*.

11. D. Deng, A.S. Argon, and S. Yip: (II), submitted to *Acta Metall.*.

12. D. Deng, A.S. Argon, and S. Yip: (III), submitted to *Acta Metall.*.

13. M. Born and K. Huang, "Dynamical Theory of Crystal Lattices", Clarendon Press: Oxford), p. 129 (1954).

14. K. Maeda and S. Takeuchi, *J. Phys. F: Met. Phys.*, *12*, 2767 (1982).

15. D. Weaire, M.F. Ashby, J. Logan, and M.J. Weins, *Acta Metall.*, *12*, 779 (1971).

16. L.A. Davis, in "Metallic Glasses" (ASM: Metals Park, Ohio), p. 190 (1978).

17. A.S. Argon, *J. Phys. Chem. Solids*, *43*, 945 (1982).

18. A.S. Argon, in "Strength of Metals and Alloys", edited by H.J. McQueen et al. (Pergamon Press: Oxford), vol. 3, p. 2007 (1986).

19. D. Deng and B. Lu, *Scripta Metall.*, *17*, 515 (1983).

20. A.S. Argon, J. Megusar, and N.J. Grant, *Scripta Metall.*, *19*, 591 (1985).

21. D. Deng and A.S. Argon *Acta Metall.*, *34*, 2011 (1986).

22. D. Deng and A.S. Argon *Acta Metall.*, *34*, 2025 (1986).

23. P.S. Steif, F. Spaepen, and J.W. Hutchinson, *Acta Metall.*, *30*, 447 (1982).

24. P. Chaudhari, F. Spaepen, and P. Steinhardt, in "Glassy Metals II", edited by H. Beck and H.J. Guntherodt (Springer: Berlin), p. 127 (1983).

25. L.T. Shi and P. Chaudhari *Phys. Rev. Lett.*, *51*, 1581 (1983).

26. J. Megusar, A.S. Argon, and N.J. Grant, *Mater. Sci. Engrg.*, *38*, 63 (1979).

27. T.M. Ahn and J.C.M. Li *Scripta Metall.*, *14*, 1057 (1980).

28. H. Koizumi and T. Ninomiya, *J. Phys. Soc. Japan*, *44*, 898 (1978).

29. H. Koizumi and T. Ninomiya *J. Phys. Soc. Japan*, *49*, 1022 (1980).

30. F.R.N. Nabarro, "Theory of Crystal Dislocations" (Clarendon Press: Oxford), p. 688 (1967).

31. D. Kuhlmann-Wilsdorf *Phys. Rev.*, *140*, A1599 (1965).

32. I.A. Kotze and D. Kuhlmann-Wilsdorf *Phil. Mag.*, *23*, 1133 (1971).

33. D. Cherns, M.L. Jenkins, and S. White, in "Electron Microscopy and Analysis, 1979" (Institute of Physics: London), p. 121 (1980).

34. A.I. Taub and F. Spaepen *Acta Metall.*, *28*, 1781 (1980).

35. K. Maeda and S. Takeuchi *Phys. Status Solidi.*, *A49*, 685 (1978).

36. E. Fukushima and A. Ookawa *J. Phys. Soc. Japan*, *10*, 970 (1955).

37. M.H. Cohen and G.S. Grest *Phys. Rev.*, *B20*, 1077 (1979).

38. G.S. Grest and M.H. Cohen, in "Advances in Chemical Physics", edited by T. Prigogine and S.A. Rice (Wiley: New York), vol. 48, p. 455 (1981).

39. U.F. Kocks, A.S. Argon, and M.F. Ashby, "Progress in Materials Science", edited by B. Chalmers et al. (Pergamon: Oxford) (1975).

APPENDIX I

Free Energy Changes due to Transformations

A shear transformation changes the Gibbs free energy of the simulation cell in a well-known way [39], as

$$\Delta G = \Delta F - \Delta W \ , \qquad (A-1)$$

where ΔF is the Helmholtz free energy change in the transformation, and ΔW the work done as the external tractions are displaced due to the local transformation. Expansion of the expression for the Helmholtz free enrgy in Eqn. (A-1) gives

$$\Delta F = \Delta U - T\Delta S = \Delta E_k + \Delta V - T\Delta S \ , \qquad (A-2)$$

where ΔU is the internal energy change which can be divided further into a change in potential energy ΔV, and kinetic energy change ΔE_k of the atoms affected by the transformation. The entropy change ΔS is primarily of a vibrational nature. In the MD method, the ΔE_k is given by

$$\Delta E_k = \frac{1}{2} m \sum_{i=1}^{n} \frac{1}{N\tau} \int_o^{N\tau} v_i^2(t) dt \ , \qquad (A-3)$$

where $v_i^2(t)$ is the square of the total instantaneous velocity of atom i at time t. This is integrated over the very small period of the strain increment occurring over a time of N fluctuation periods τ. The sum is carried out over all n atoms in the cluster. In the present simulation, however, the temperature was 10^{-3}, and therefore, ($T = 4\text{x}10^{-3}\text{T}_\text{m}$ in units of E_o/k. This makes the average level of kinetic energy per atom $10^{-3}E_o$, while the average potential energy per atom is around $2E_o$ (see Fig. 11a). Thus, the kinetic energy and its changes are totally negligible in this simulation, and can be ignored. The vibrational entropy contributions to the free energy in systems where the energy is derived from elastic strain energy is usually accounted through the temperature dependence of the elastic constants which enter into the statement of the elastic energy changes. Here, again, because of the very low level of the temperature in the simulation, the entropy contributions to the free energy can also be neglected. This leaves for the Gibbs free energy change:

$$\Delta G = \Delta V - \Delta W \qquad (A-4)$$

This was what was used in the evaluations of the six clusters which were considered in detail – of which two are plotted in Figs. 18a and 18b.

FIGURE CAPTIONS

Fig. 1 Change of volume per atom in simulation cell with temperature in the large system of 780 atoms: (o) increasing temperature (□) decreasing temperature.

Fig. 2 (a) Distorted Voronoi polygons in the two-dimensional two-component material at its melting point of $T^* = 0.25$ on a normalized temperature scale, (b) the atomic structure of the same material shown in (a) after quenching to $T^* = 10^{-3}$ and relaxing for 4000 time steps. Note the liquid-like material of 5-7 sided polygons separating quasi-ordered regions.

Fig. 3 Radial distribution function of atom positions in the as-quenched glass shown in Fig. 2b.

Fig. 4 Sequence of *enthalpy* relaxation in the simulation mat of the 2-D material shown in Fig. 2b, following a small shear strain increment of 5×10^{-4}. Note that the most rapid early relaxation is complete, after 190 time steps.

Fig. 5 (a) Dependence of external cell pressure on volume change (area change), (b) dependence of shear stress on the cell, on volume change.

Fig. 6 Pressure dependence of the two-dimensional bulk modulus derived from the information in Fig. 5.

Fig. 7 The shear stress-shear strain curve of the model atomic glass sheared isothermally at $T^* = 10^{-3}$.

Fig. 8 Portion of the forward shear stress-shear strain curve and three curves for reverse deformation, initiated at forward shear strains of 0.025, 0.075, and 0.125. Note, the very prominent Bauschinger effects.

Fig. 9 Increase in evoked pressure on the simulation cell due to deformation induced volume increase.

Fig. 10 Effect of deformation reversals on the evoked pressure. Note dips in evoked pressure with reverse deformations initiated at forward shear strains of 0.075 and 0.125.

Fig. 11 (a) Change in potential energy per atom (enthalpy per atom) in dimensionless units of energy as a function of shear strain. The close parallel of this behavior to that of the pressure shown in Fig. 9 indicates that the increases in enthalpy are due to the dilatancy effect, (b) changes in the potential energy upon deformation reversals.

Fig. 12 Radial distribution function of atom positions of the simulation cell after a shear strain of 0.1.

Fig. 13 Incremental displacement field of atoms due to a shear strain of $5x10^{-4}$ at a total shear strain of 0.051. Note several of the clusters undergoing cooperative deformation.

Fig. 14 (a) Local atomic level maximum shear spikes, regardless of principal axis orientation in the simulation field for an external imposed shear strain increment of $5x10^{-4}$ at a total shear strain level of 0.051, (b) the corresponding atomic site dilatations associated with the shear strain increment of (a).

Fig. 15 (a) Distribution of atomic site maximum shear stress, (b) distribution of atomic site pressure (Δ) and negative pressure (∇), (c) distribution of free volume among atom sites, (d) distribution of atomic site distortion parameter; all at a total shear strain of 0.051 considered as description of the initial state for a subsequent increment of shear strain of $5x10^{-4}$.

Fig. 16. Distribution of local atomic level $x - y$ shear strain increments during an externally imposed shear strain increment of $5x10^{-4}$, at a total shear strain of 0.051.

Fig. 17. The distribution of $x - y$ shear strains of positive and negative sign occurring during an externally imposed shear strain increment of $5x10^{-4}$ at a total shear strain of 0.051, the squares are strain spikes, and are in the same direction as the applied strain increment, the diamonds are of negative sign.

Fig. 18 The specific history plots of two separate clusters showing the monotonic decrease in Gibbs free energy accompanying a monotonic rise in shear strain: (a) cluster shearing in the same direction as external shear increment, (b) cluster shearing in the opposite direction.

Fig. 19 Frequency distribution of free energy barriers on the monotonic decrease of the Gibbs free energies in deforming clusters, as obtained from history plots of the type shown in Figs. 18a and 18b.

Fig. 20 Distribution of local total $x - y$ shear strains in the initial apparent elastic response range: (a) at a total shear strain of 0.0125, (b) at a strain of 0.025, (c) at a strain of 0.05.

Fig. 21 Sequence of development of shear localization in the simulation cell due to the accumulated effect of deformation induced dilatations (a) $\gamma = 0.05$, (b) $\gamma = 0.10$, (c) $\gamma = 0.20$.

Fig. 22 Distribution of deformation induced local volume changes during externally imposed strain increments of $5x10^{-4}$ at total strains of: (a) $\gamma = 0.05$, (b) $\gamma = 0.10$, (c) $\gamma = 0.15$, and (d) $\gamma = 0.20$.

Fig. 23 Distribution of total accumulated local dilatations at atom sites at total strains of: (a) $\gamma = 0.05$, (b) $\gamma = 0.10$, (c) $\gamma = 0.15$, and (d) $\gamma = 0.20$.

Fig. 24. Deformation induced changes in the distribution of liquid-like material represented by the boundaries of 5-7 sided polygons: (a) after a total strain of $\gamma = 0.05$, note a dipole of two-edge dislocations at site marked A, (b) after $\gamma = 0.10$, note the separation of the two-edge dislocations from the dipole configuration, (c) after $\gamma = 0.15$, note that the left-hand dislocation has now entered the cell from the right side, (d) after $\gamma = 0.20$.

Fig. 25 Variation with strain of the total number of liquid-like material polygons with edges different than 6.

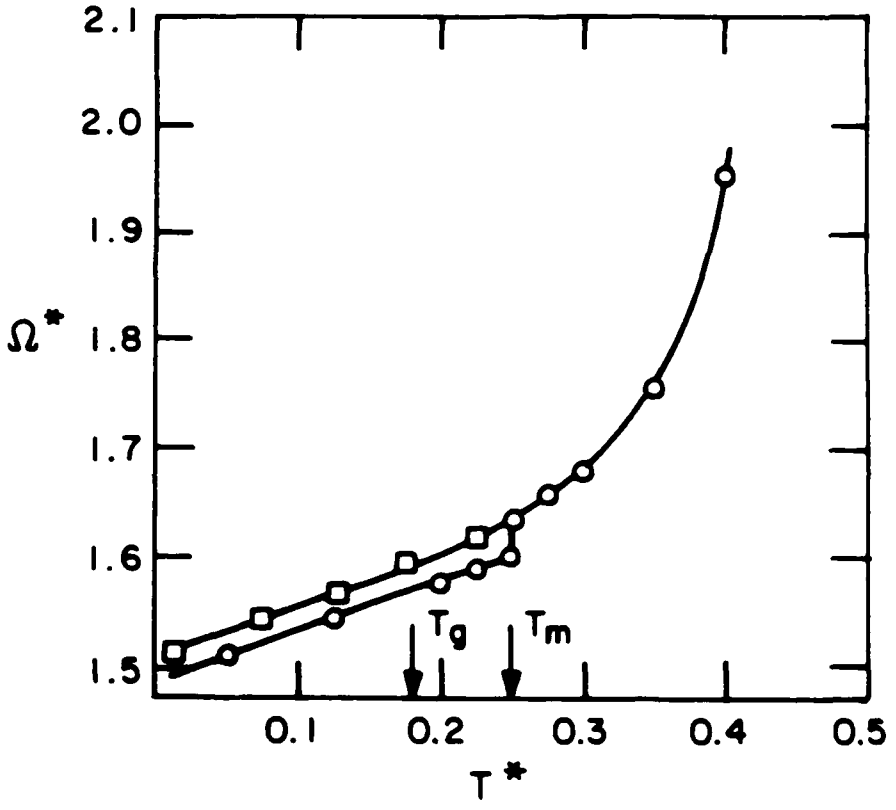

Fig. 1 - Change of volume per atom in simulation cell with temperature in the large system of 780 atoms: (o) increasing temperature, (□) decreasing temperature.

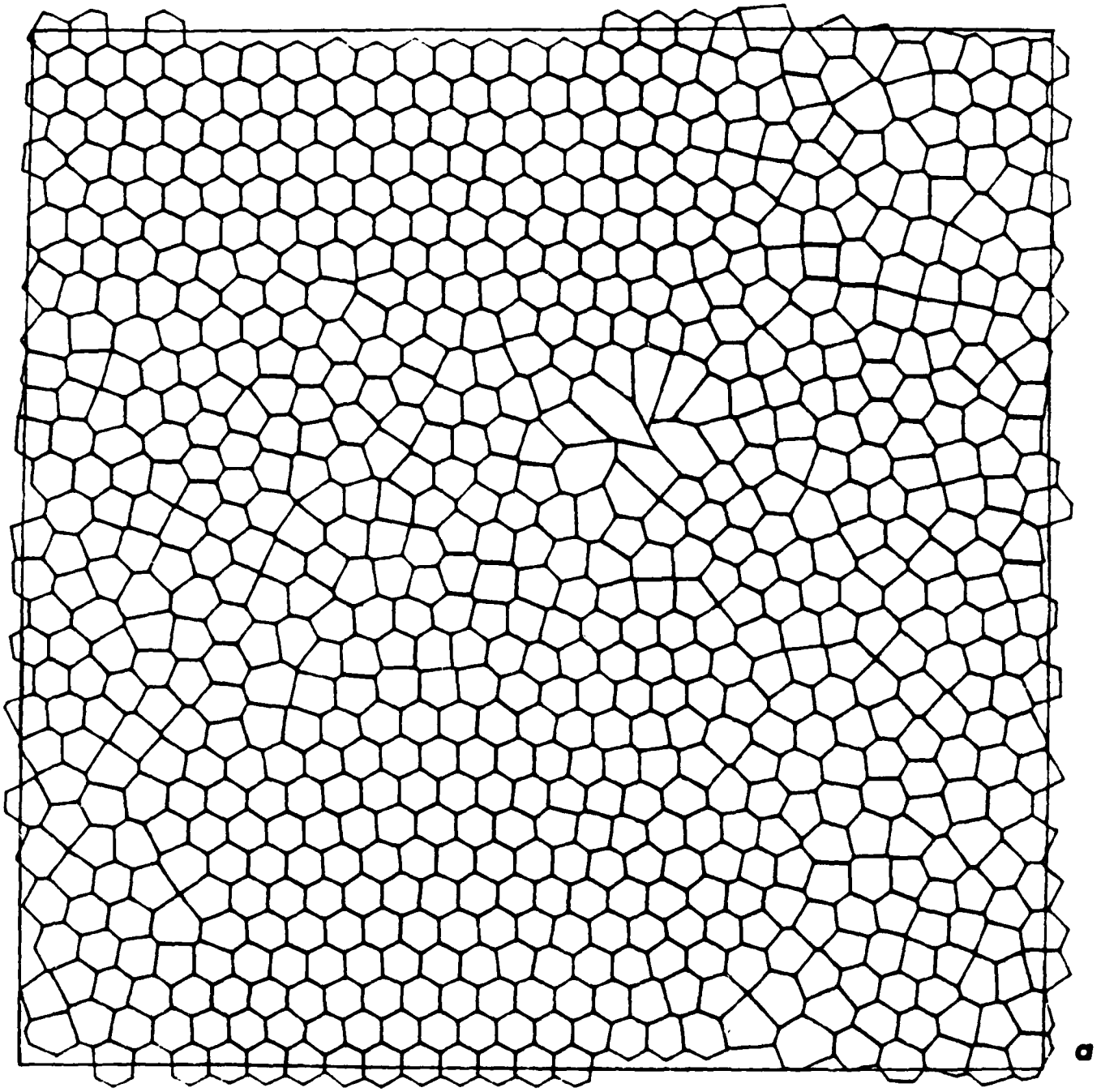

Fig. 2 - (a) Distorted Voronoi polygons in the two-dimensional two-component material at its melting point of T = 0.25 on the normalized temperature scale, (b) the atomic structure of the same material shown in (a) after quenching to T = 10^{-3} and relaxing for 4000 time steps. Note the liquid-like material of 5-7 sided polygons separating quasi-ordered regions.

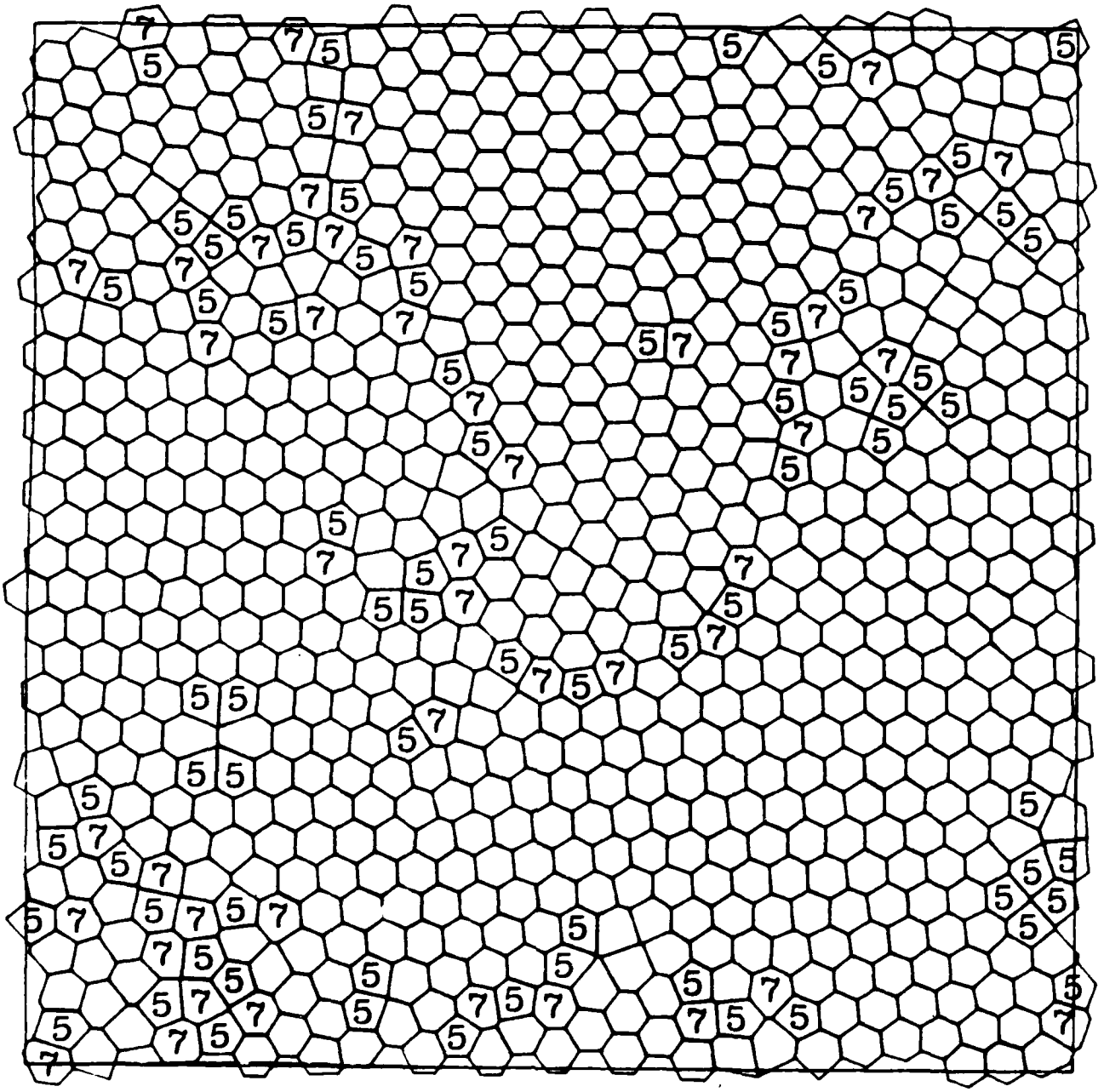

Fig. 2b

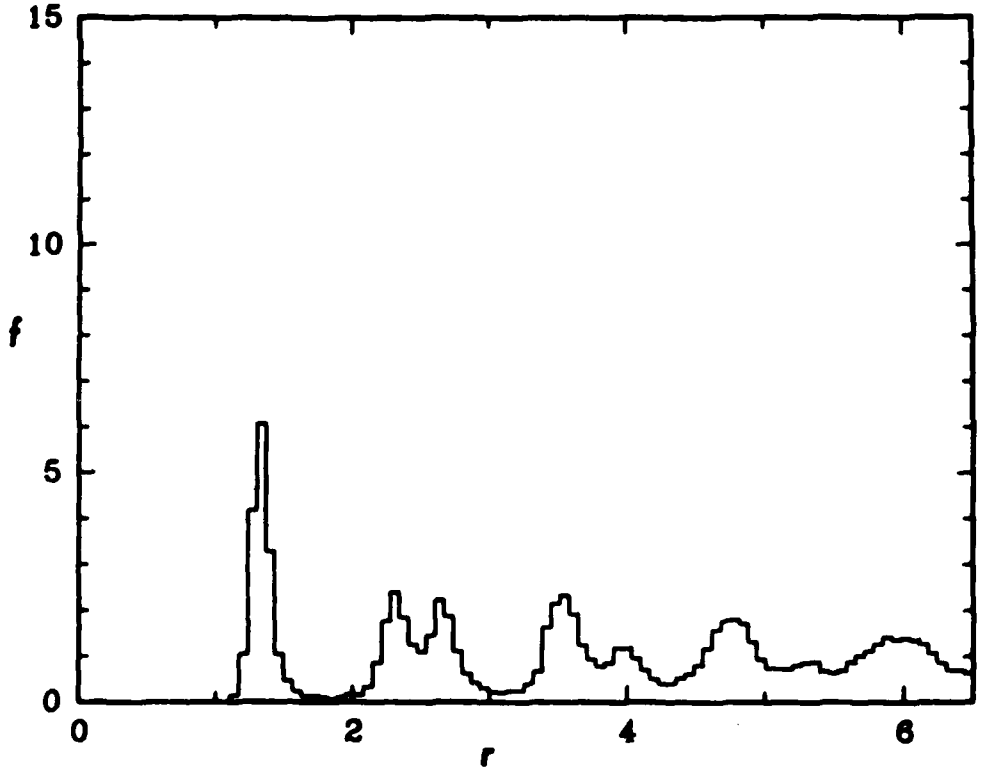

Fig. 3 - Radial distribution function of atom positions in the as-quenched glass shown in Fig. 2b.

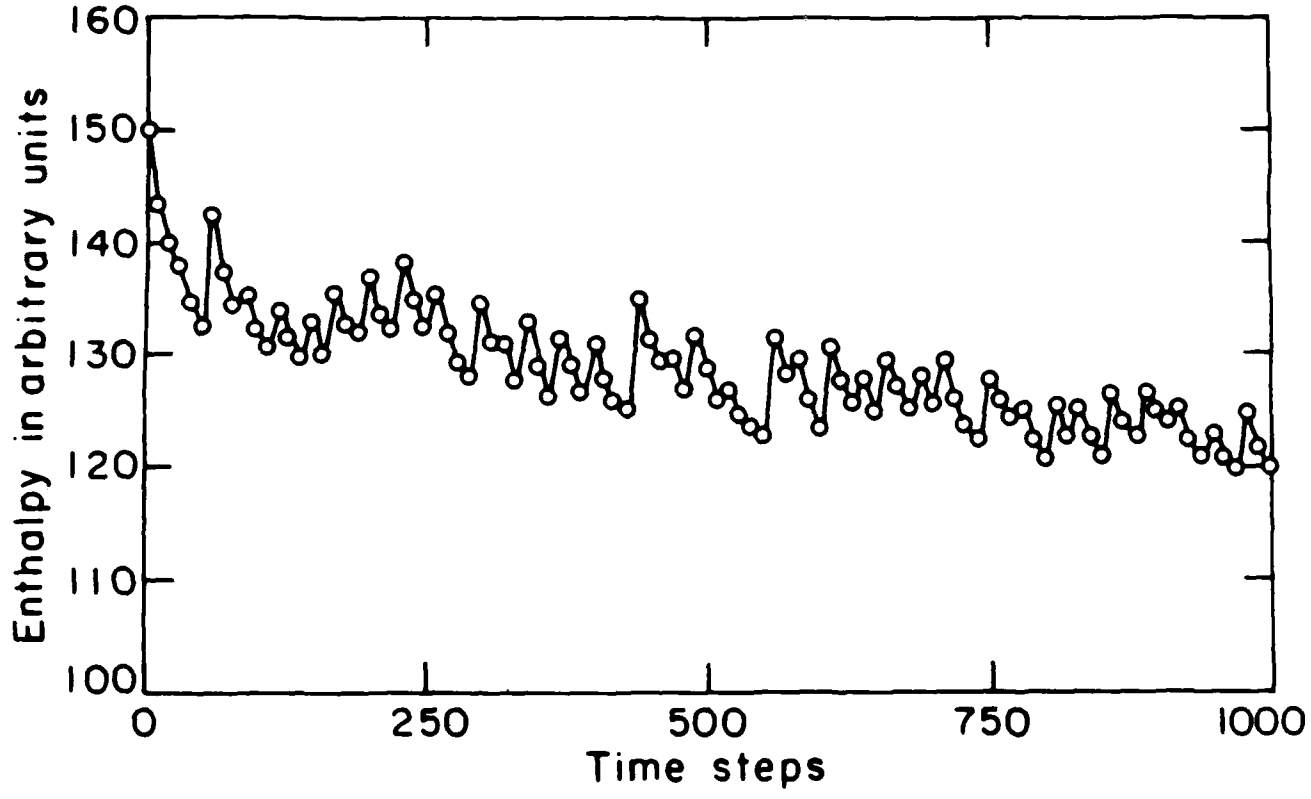

Fig. 4 - Sequence of enthalpy relaxation in the simulation mat of the 2-D material shown in Fig. 2b, following a small shear strain increment of 5×10^{-4}. Note that the most rapid early relaxation is complete, after 190 time steps.

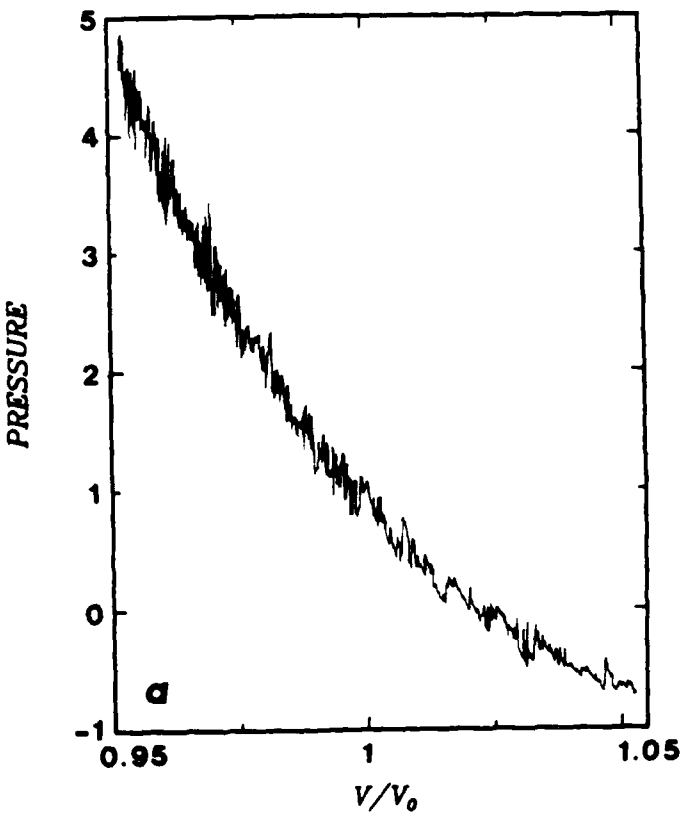

Fig. 5 - (a) Dependence of external cell pressure on volume change (area change), (b) dependence of shear stress on the cell, on volume change.

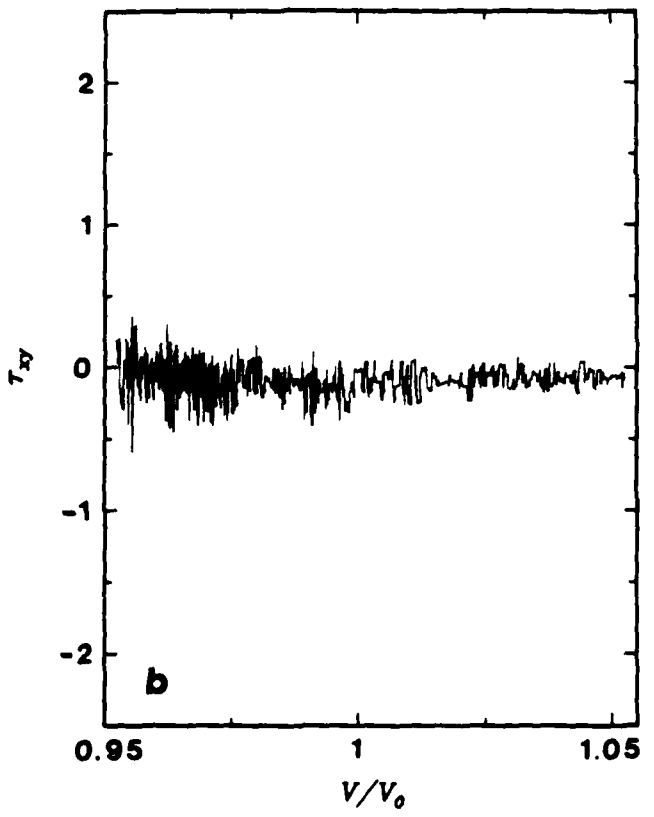

Fig. 5b

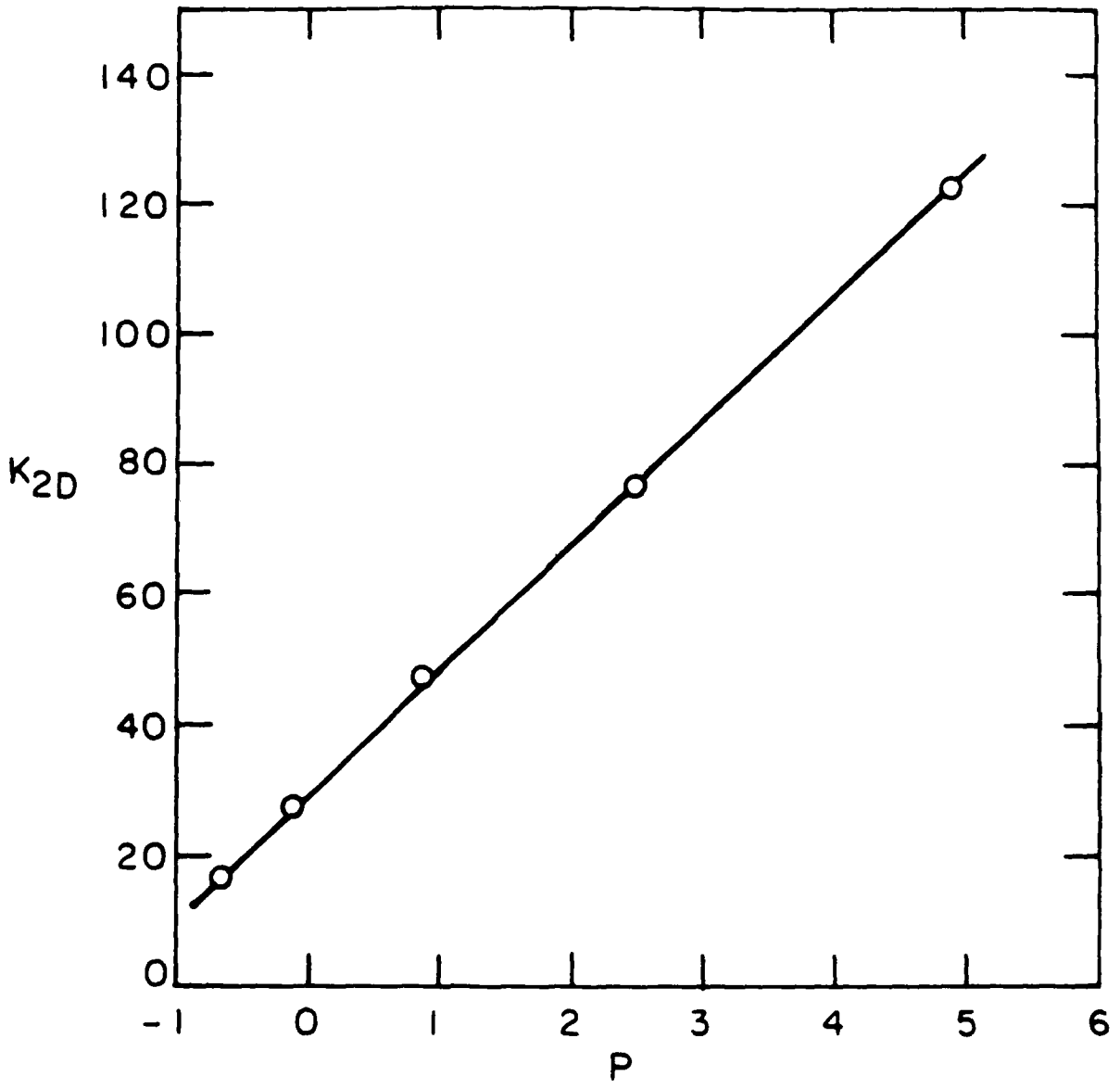

Fig. 6 - Pressure dependence of the two-dimensional bulk modulus derived from the information in Fig. 5.

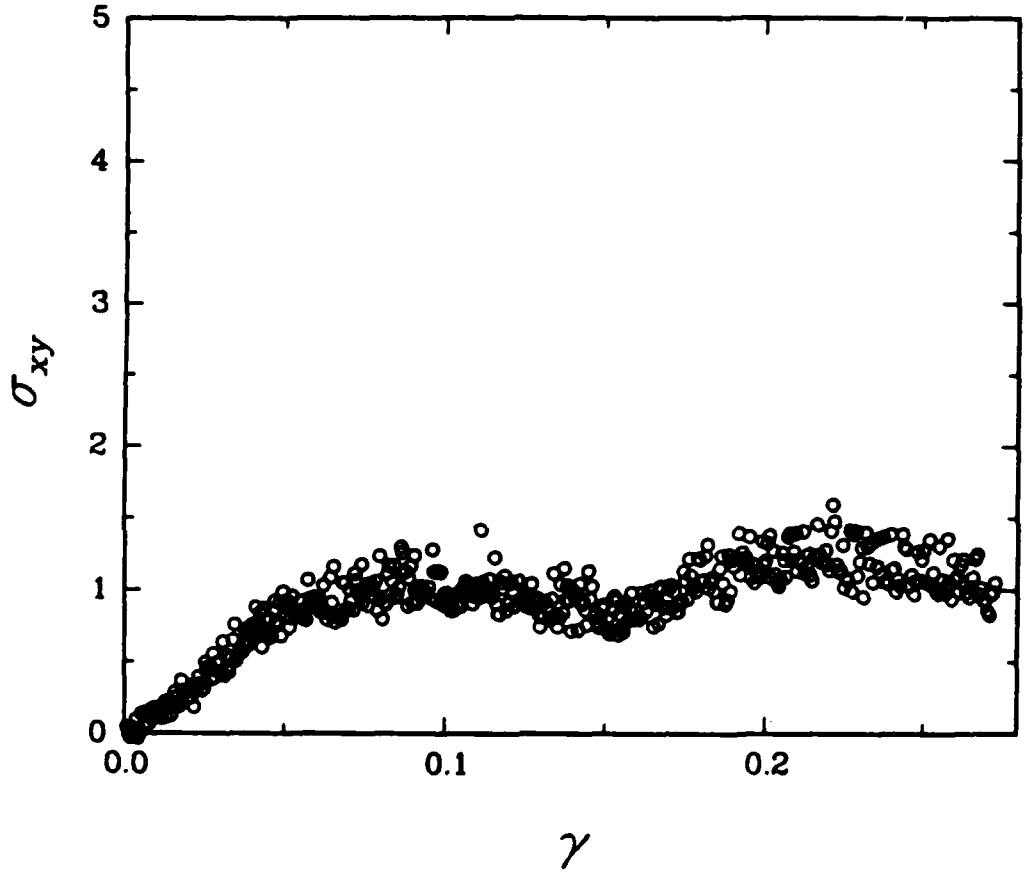

Fig. 7 - The shear stress-shear strain curve of the model atomic glass sheared isothermally at $T^* = 10^{-3}$.

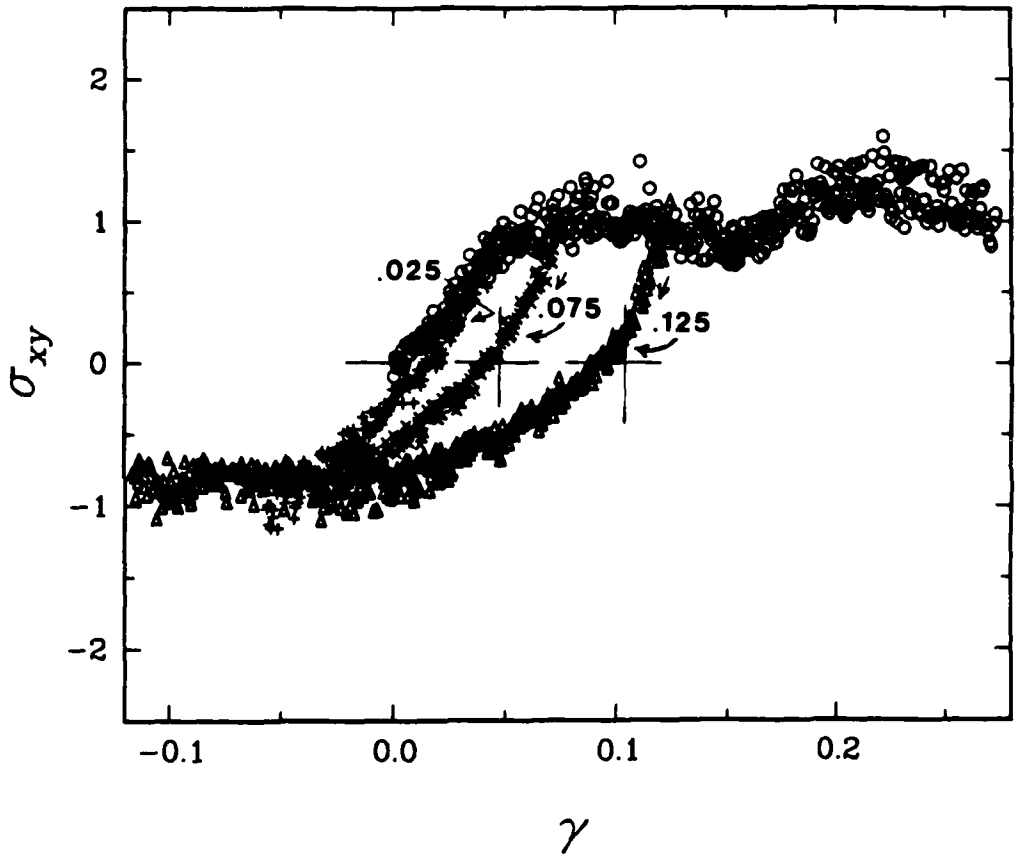

Fig. 8 - Portion of the forward shear stress-shear strain curve and three curves for reverse deformation, initiated at forward shear strains of 0.025, 0.075, and 0.125. Note, the very prominent Bauschinger effects.

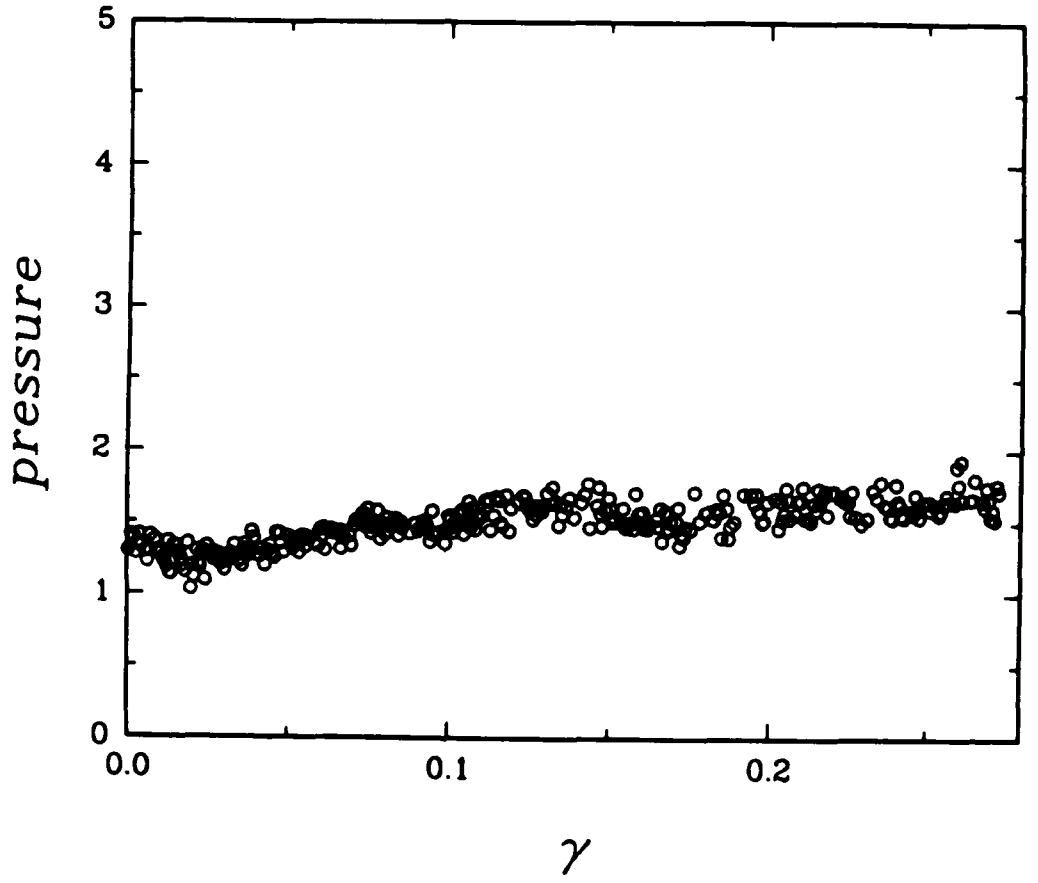

Fig. 9 - Increase in evoked pressure on the simulation cell due to deformation induced volume increase.

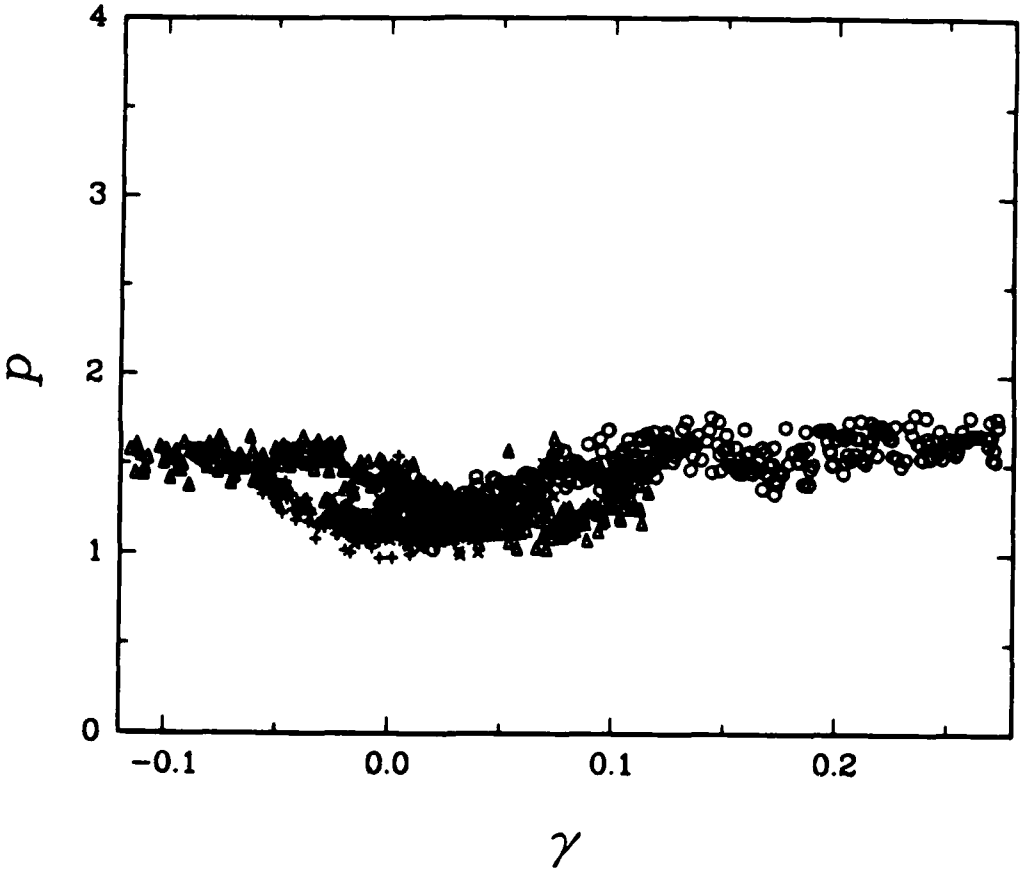

Fig. 10 - Effect of deformation reversals on the evoked pressure. Note dips in evoked pressure with reverse deformations initiated at forward shear strains of 0.075 and 0.125.

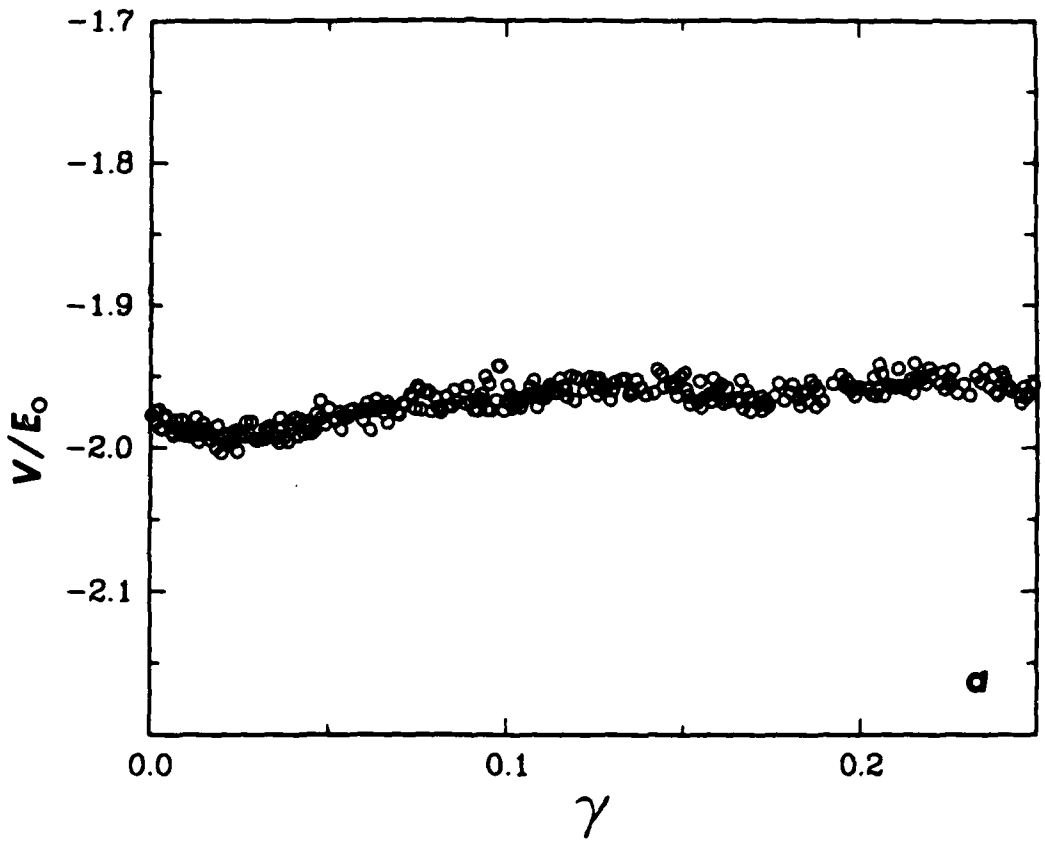

Fig. 11 - (a) Change in potential energy per atom (enthalpy per atom) in dimensionless units of energy as a function of shear strain. The close parallel of this behavior to that of the pressure shown in Fig. 9 indicates that the increases in enthalpy are due to the dilatancy effects, (b) changes in the potential energy upon deformation reversals.

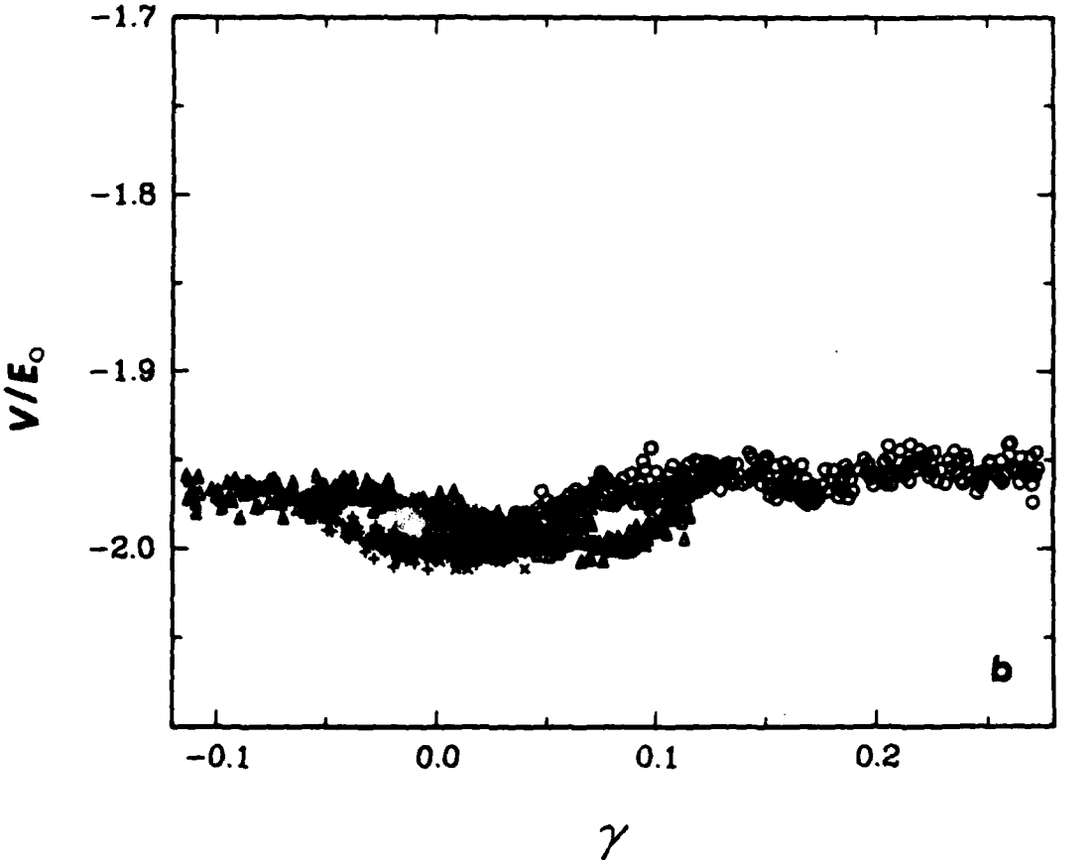

Fig. 11b

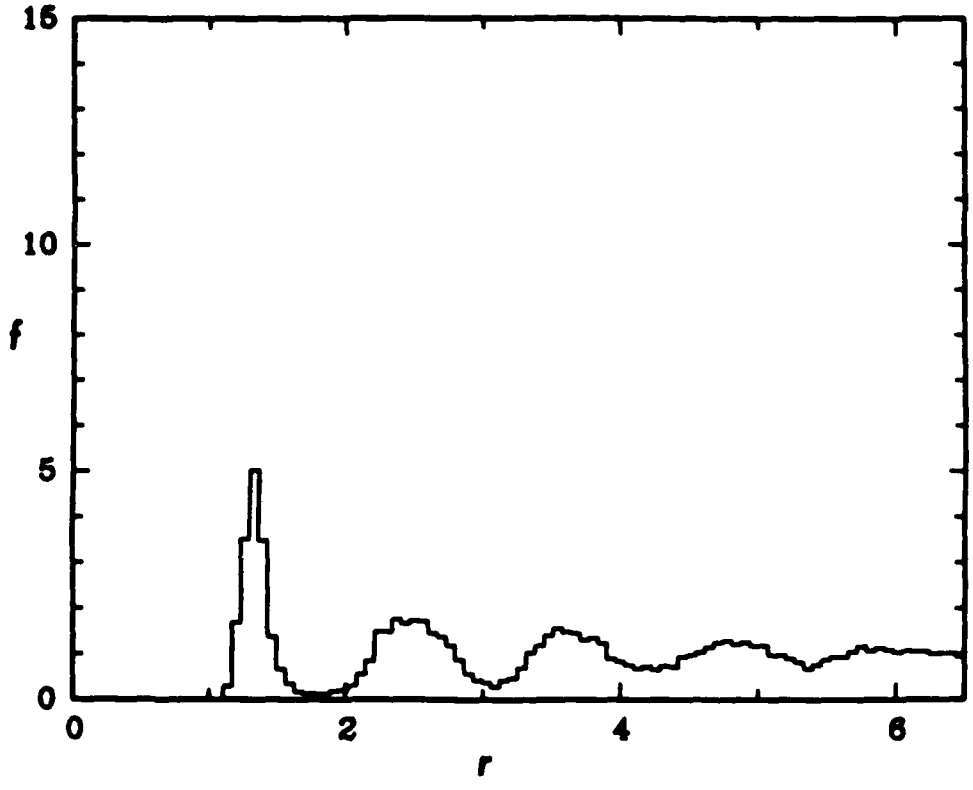

Fig. 12 - Radial distribution function of atom positions of the simulation cell after a shear strain of 0.1.

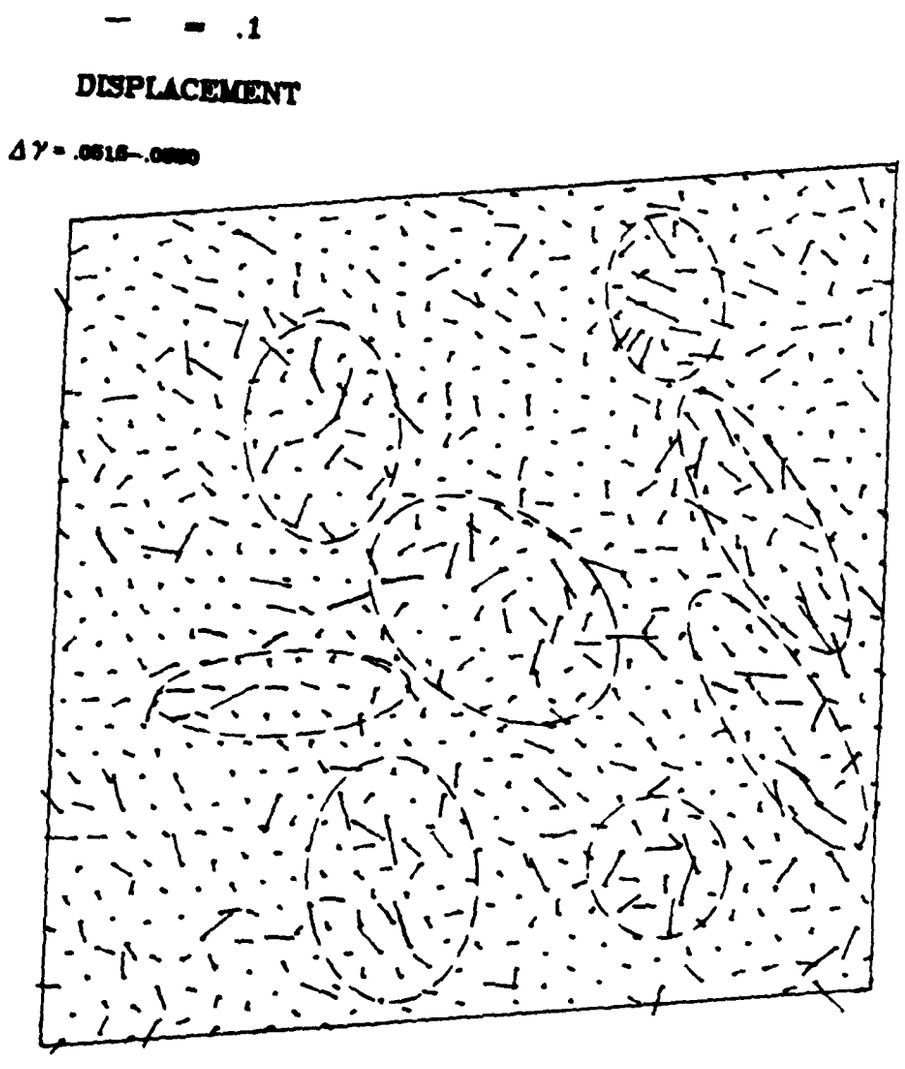

Fig. 13 - Incremental displacement field of atoms due to a shear strain of 5×10^{-4} at a total shear strain of 0.051. Note several of the clusters undergoing cooperative deformation.

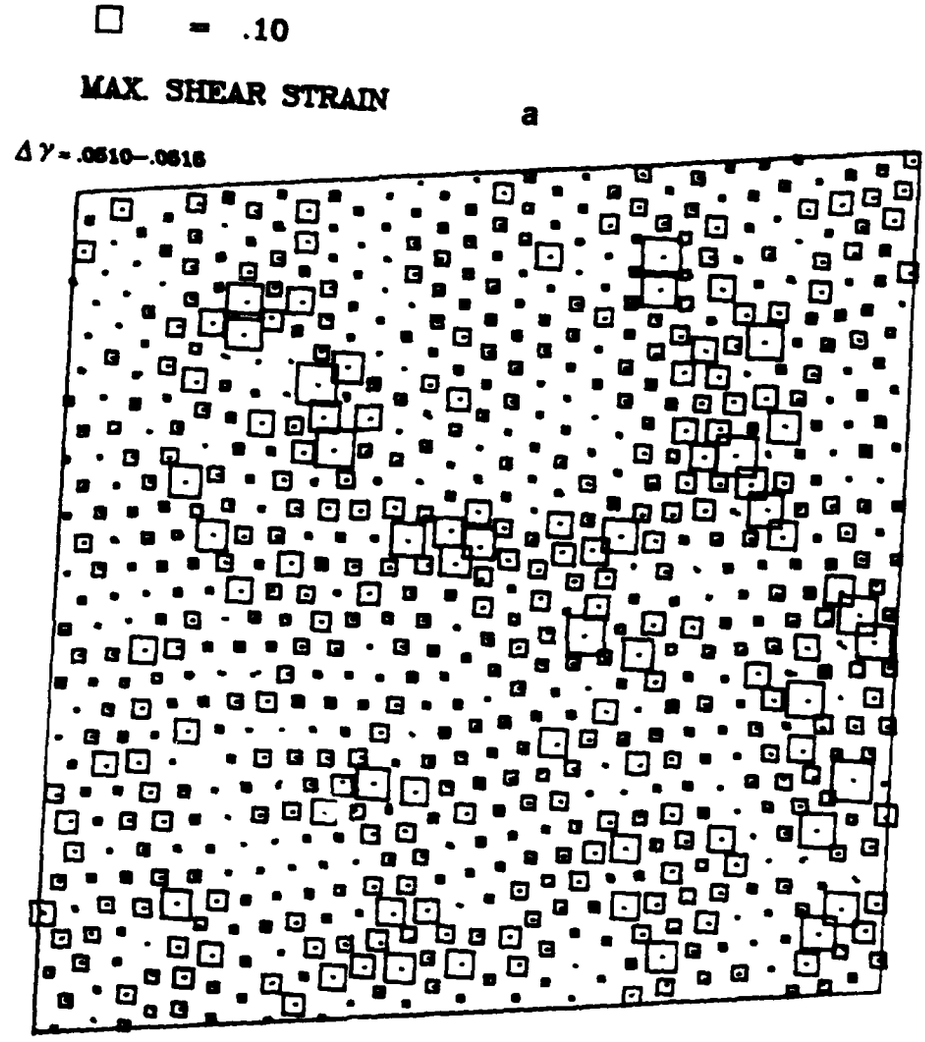

Fig. 14 - (a) Local atomic level maximum shear spikes, regardless of principal axis orientation in the simulation field for an external imposed shear strain increment of 5×10^{-4} at a total shear strain level of 0.051, (b) the corresponding atomic site dilatations associated with the shear strain increment of (a).

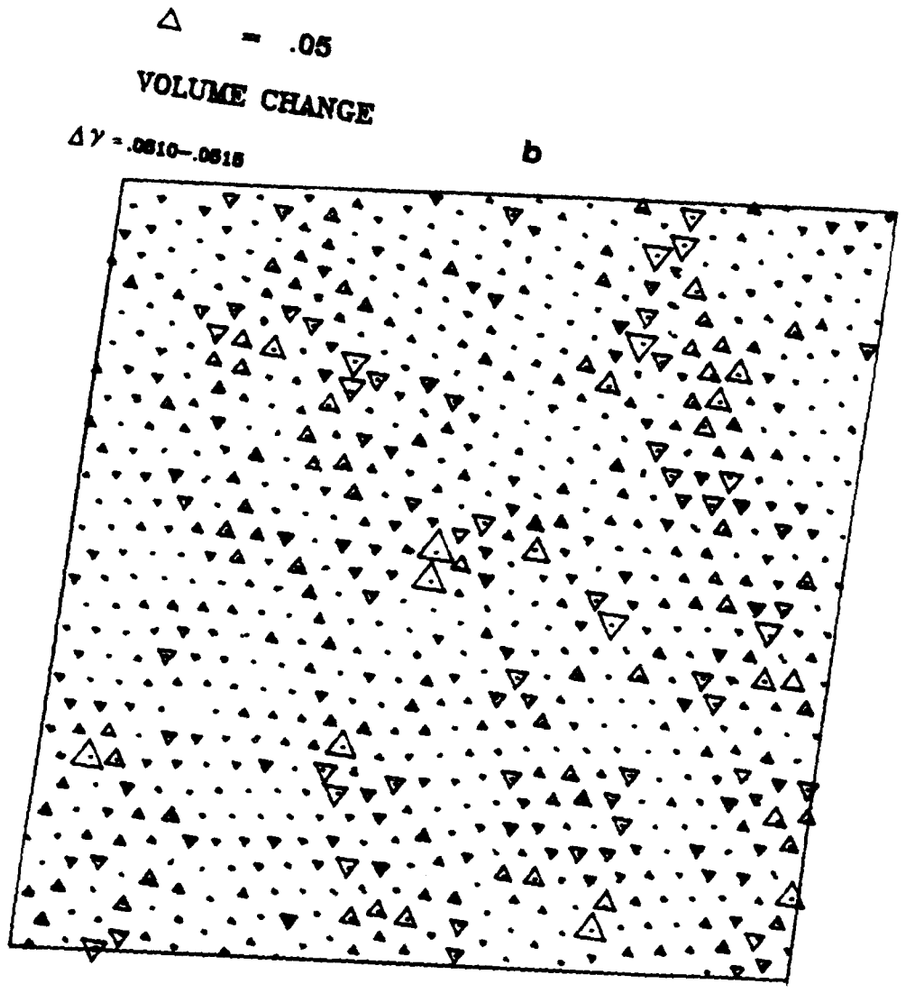

Fig. 14b

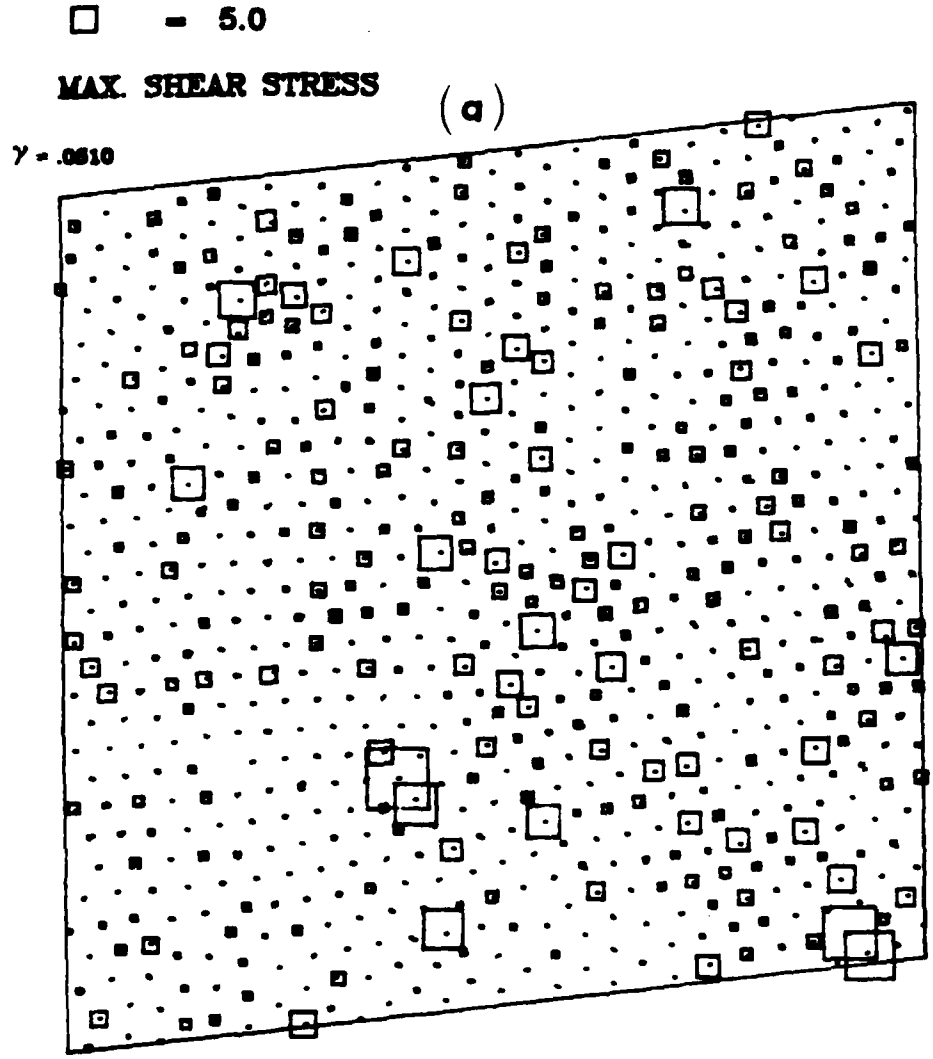

Fig. 15 - (a) Distribution of atomic site maximum shear stress, (b) distribution of atomic site pressure (△) and negative pressure (▽), (c) distribution of free volume among atom sites, (d) distribution of atomic site distortion parameter; all at a total shear strain of 0.051 considered as description of the initial state for a subsequent increment of shear strain of 5×10^{-4}.

Δ = 5.0

LOCAL PRESSURE

(b)

γ = .0810

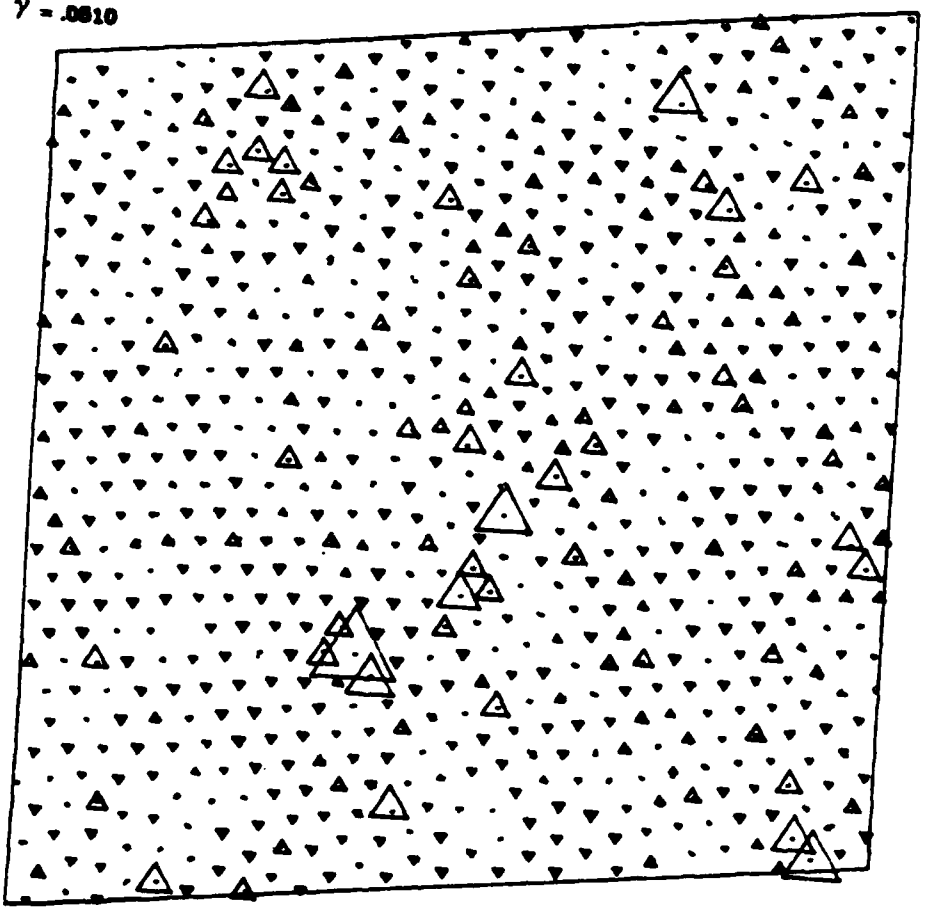

Fig. 15b

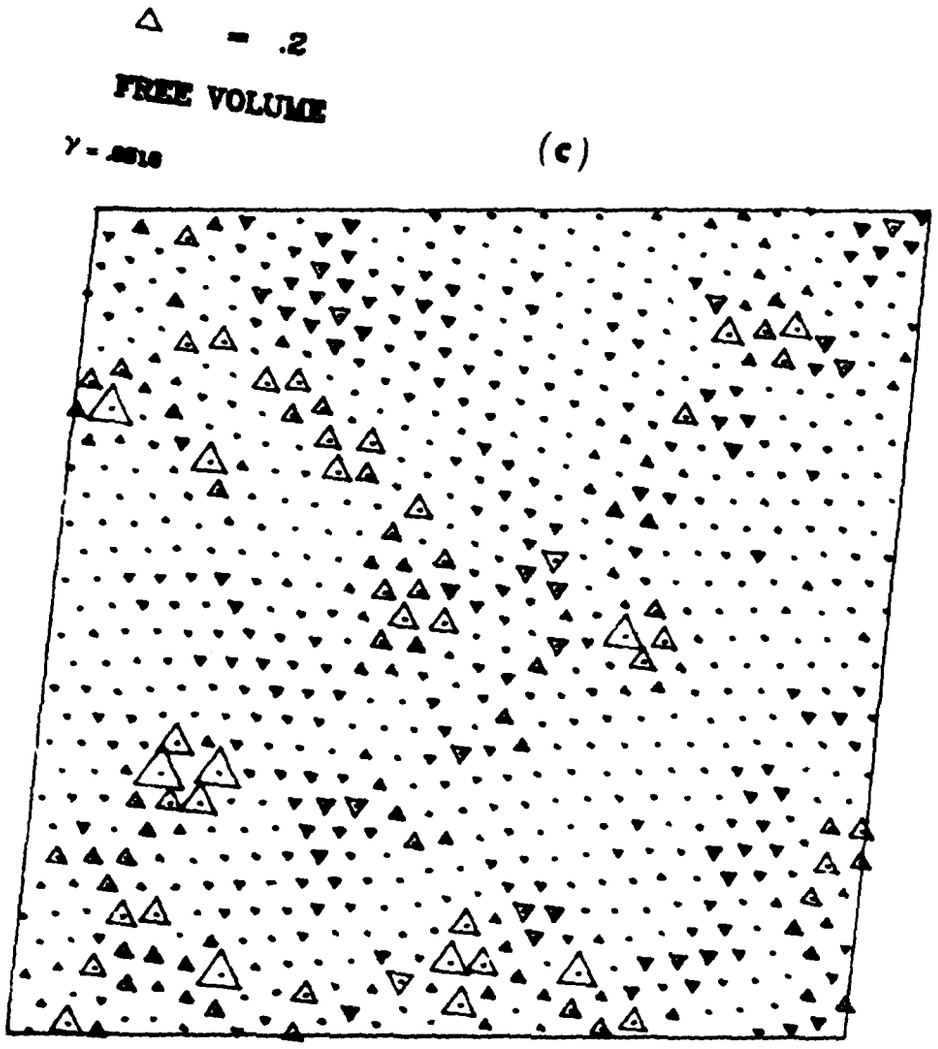

Fig. 15c

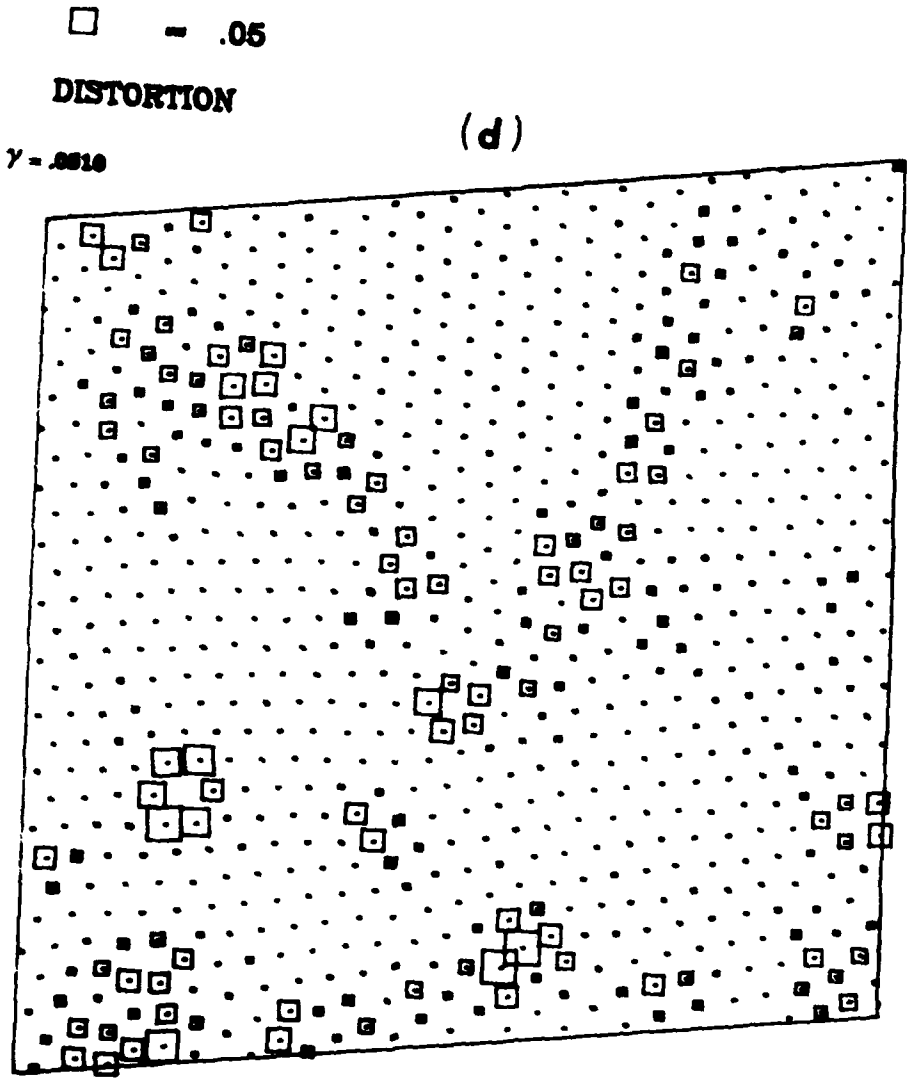

Fig. 15d

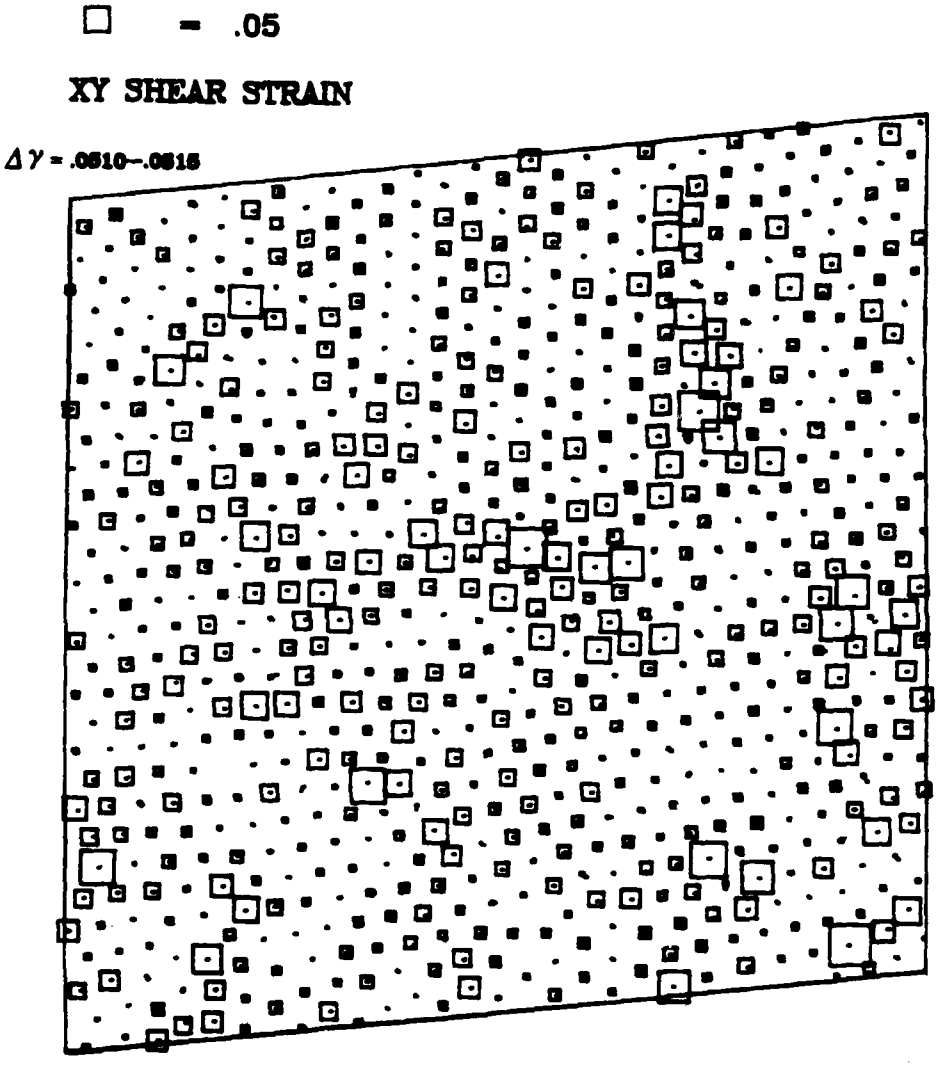

Fig. 16 - Distribution of local atomic level x-y shear strain increments during an externally imposed shear strain increment of 5×10^{-4}, at a total shear strain of 0.051.

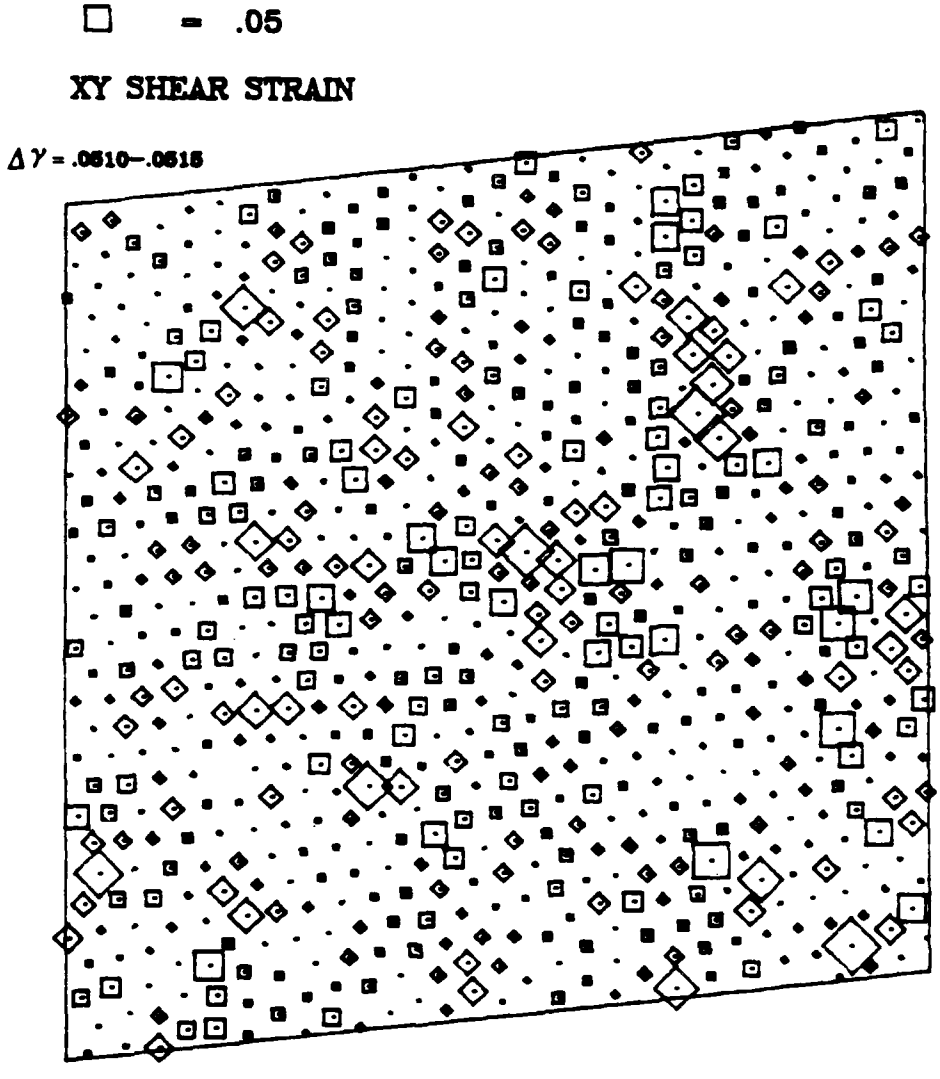

Fig. 17 - The distribution of x-y shear strains of positive and negative sign occurring during an externally imposed shear strain increment of 5×10^{-4} at a total shear strain of 0.051, the squares are strain spikes, and are in the same direction as the applied strain increment, the diamonds are of negative sign.

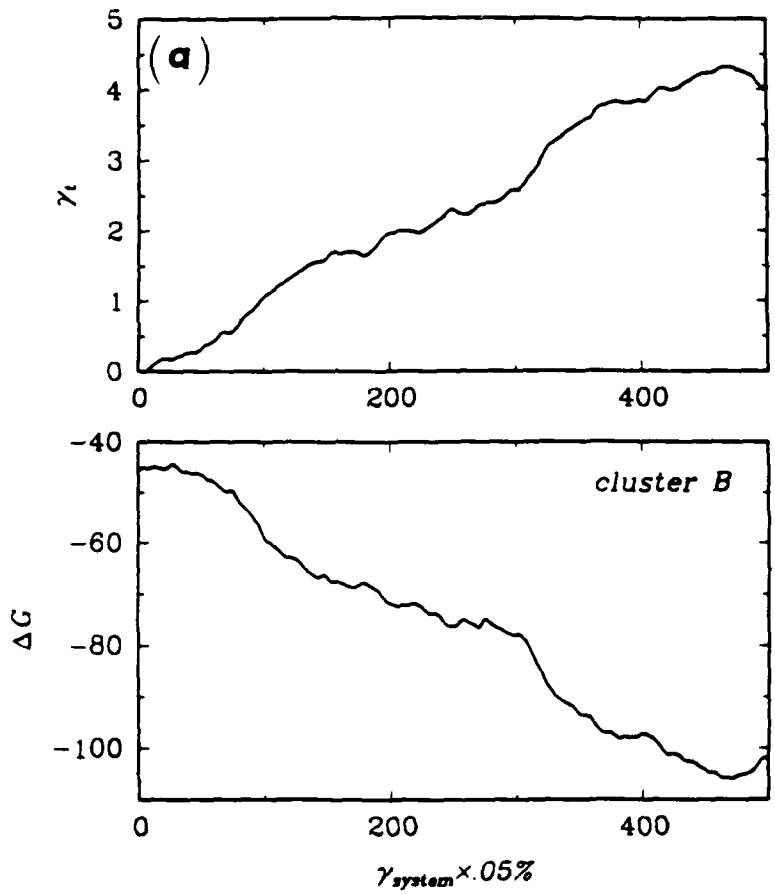

Fig. 18 - The specific history plots of two separate clusters showing the monotonic decrease in Gibbs free energy accompanying a monotonic rise in shear strain: (a) cluster shearing in the same direction as external shear increment, (b) cluster shearing in the opposite direction.

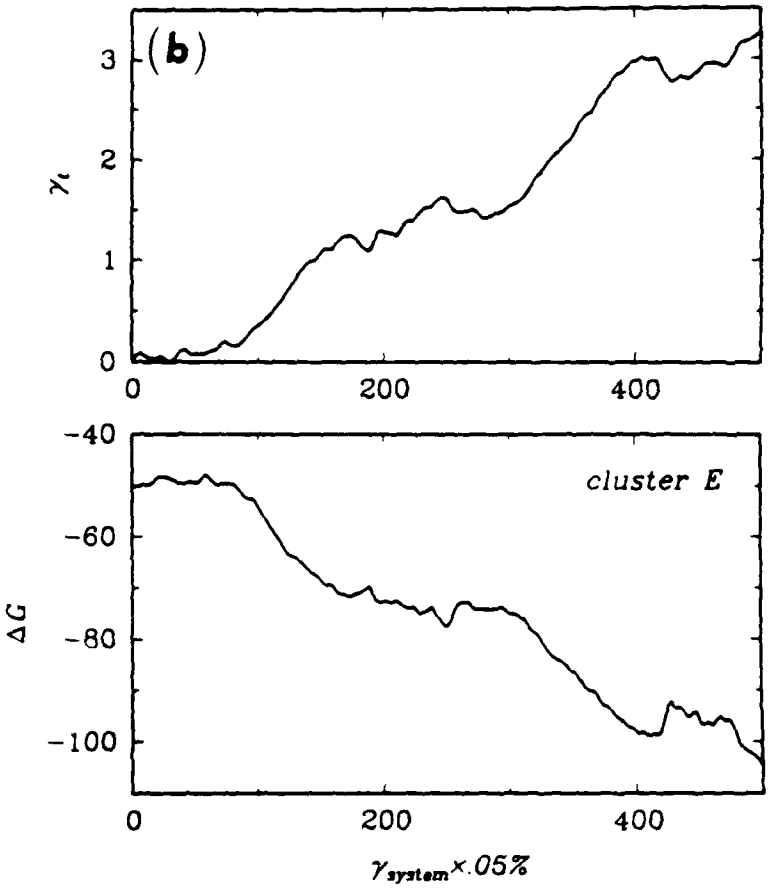
(b)
3
2
1
0
γ_t
0
200
400
-40
-60
-80
-100
ΔG
cluster E
0
200
400
$\gamma_{system} \times .05\%$

Fig. 18b

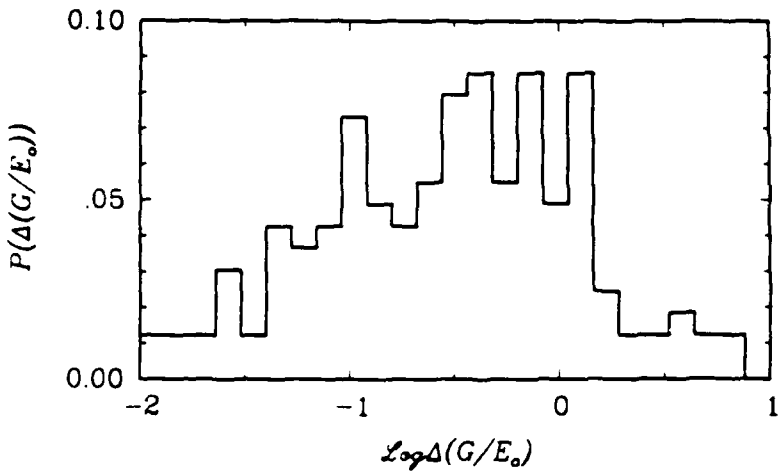

Fig. 19 - Frequency distribution of free energy barriers on the monotonic decrease of the Gibbs free energies in deforming clusters, as obtained from history plots of the type shown in Figs. 18a and 18b.

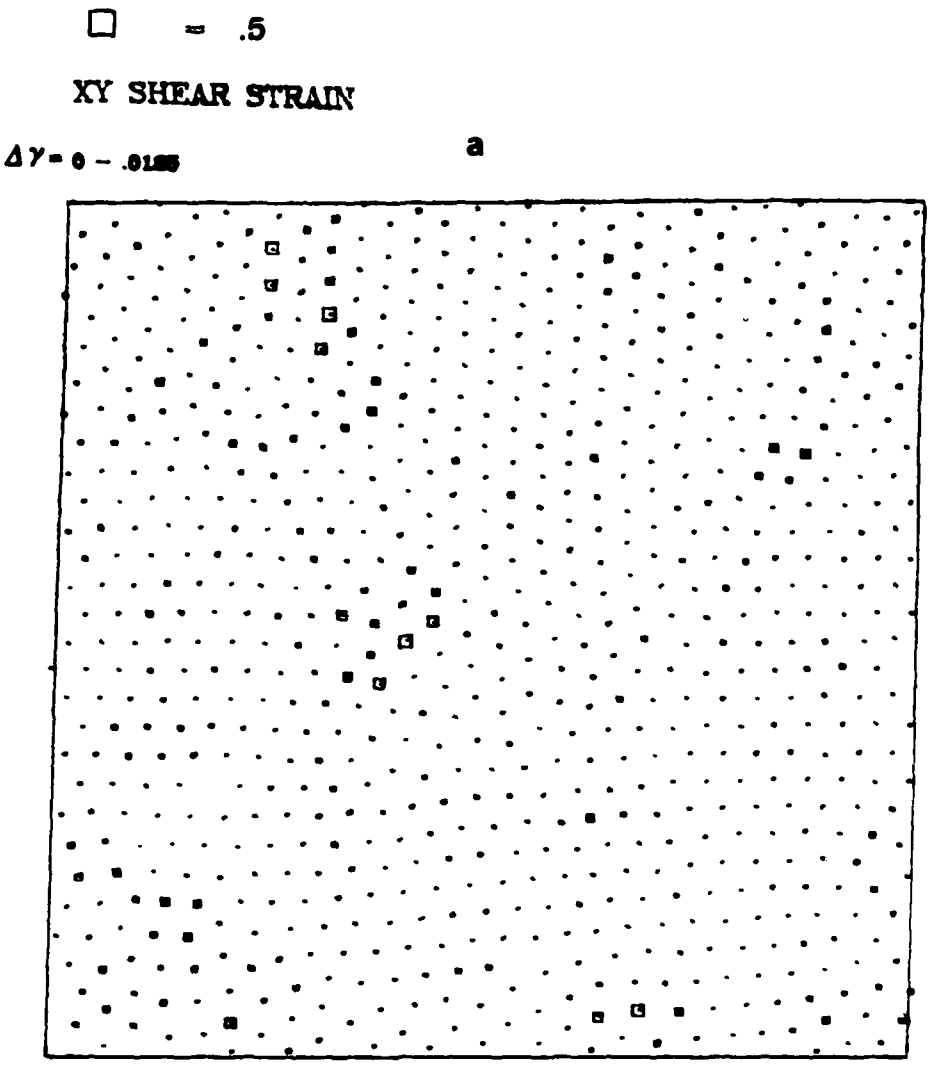

Fig. 20 - Distribution of local total x-y shear strains in the initial apparent elastic response range: (a) at a total shear strain of 0.0125, (b) at a strain of 0.025, (c) at a strain of 0.05.

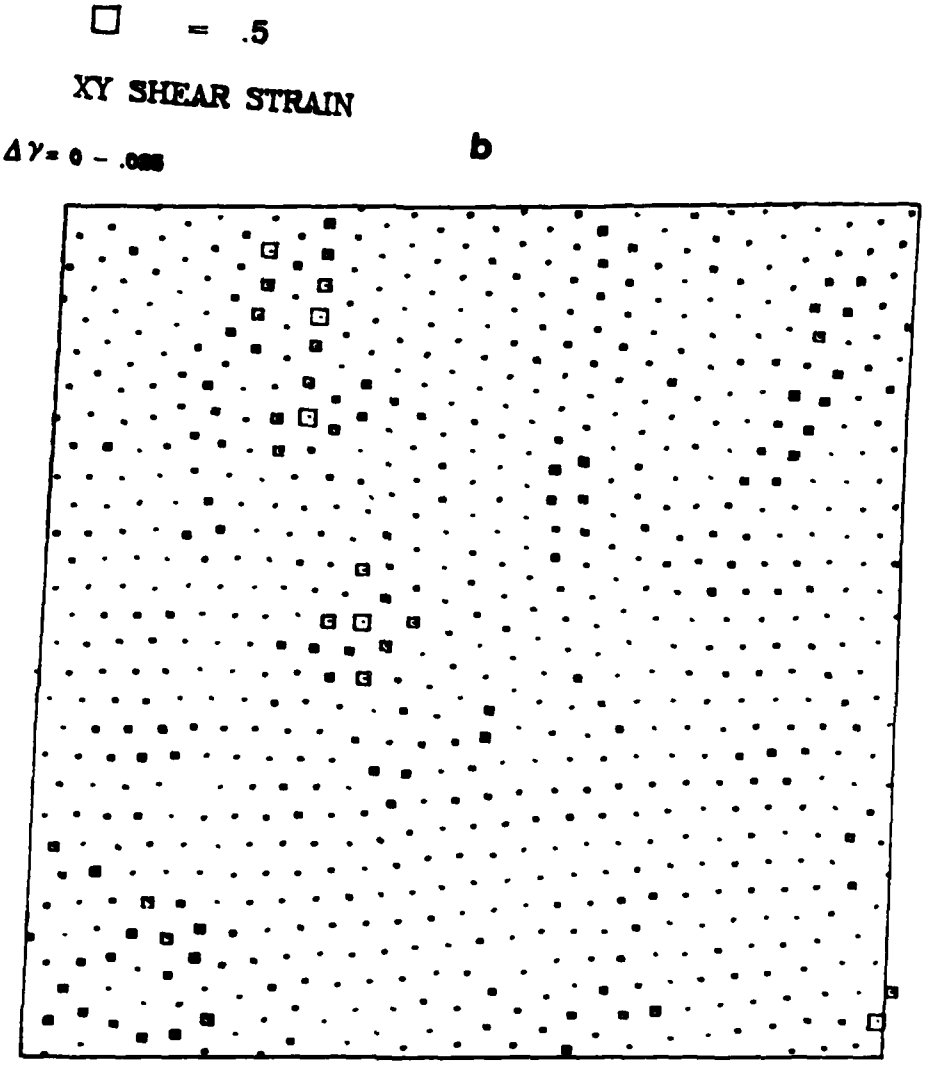

Fig. 20b

□ = .5

XY SHEAR STRAIN

$\Delta\gamma = 0 - .06$ C

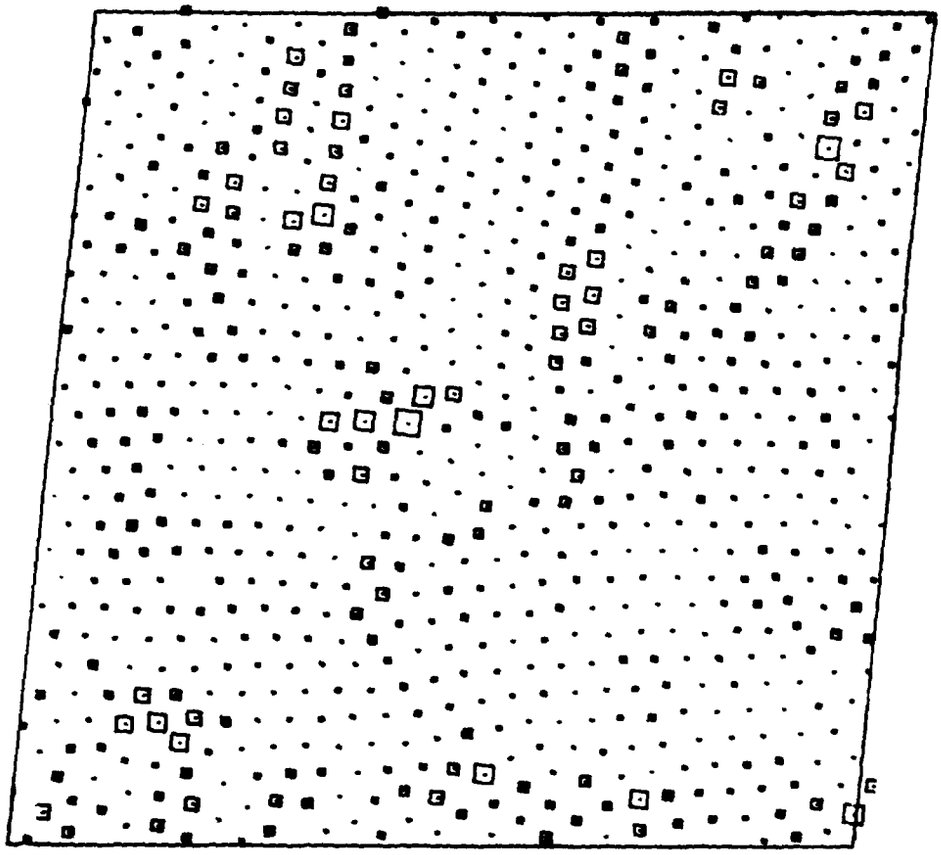

Fig. 20c

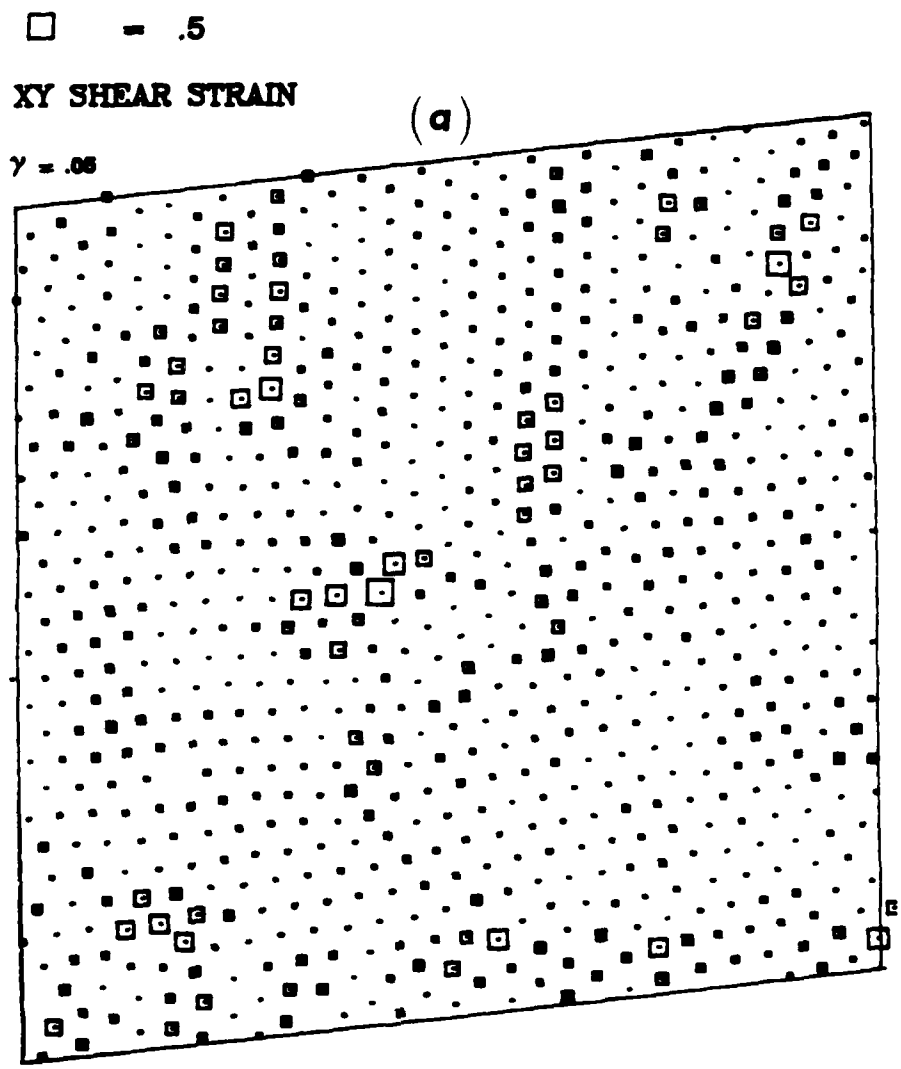

Fig. 21 - Sequence of development of shear localization in the simulation cell due to the accumulated effect of deformation induced dilatations: (a) $\gamma = 0.05$, (b) $\gamma = 0.10$, (c) $\gamma = 0.15$, and (d) $\gamma = 0.20$.

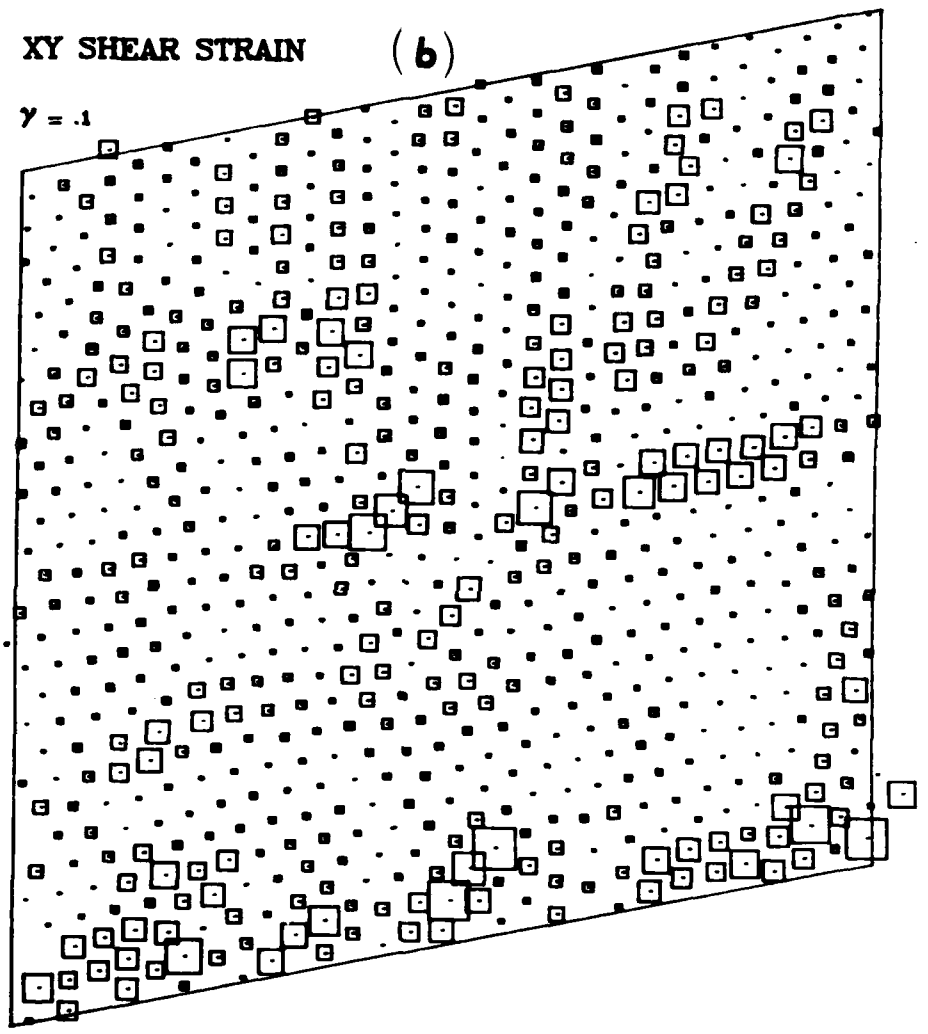

Fig. 21b

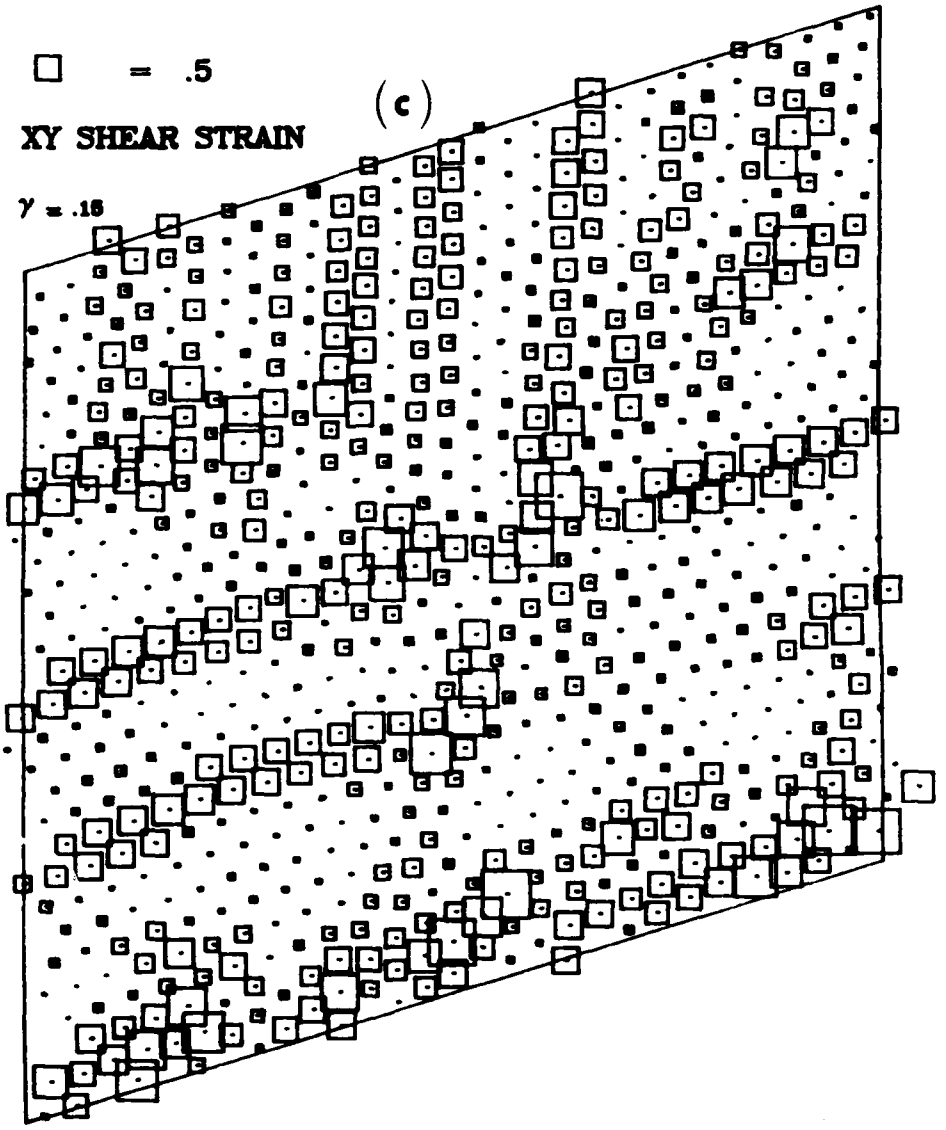

Fig. 21c

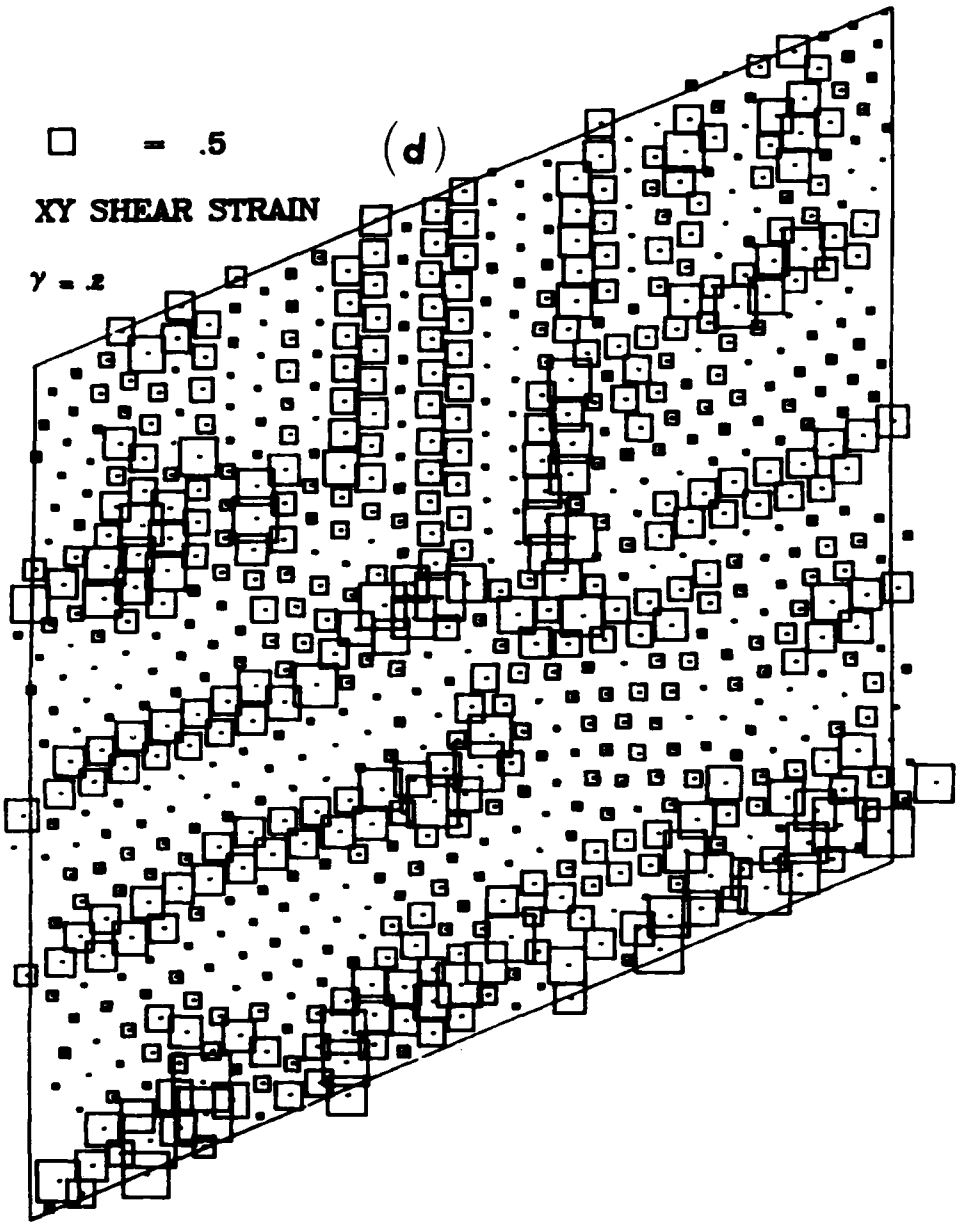

Fig. 21d

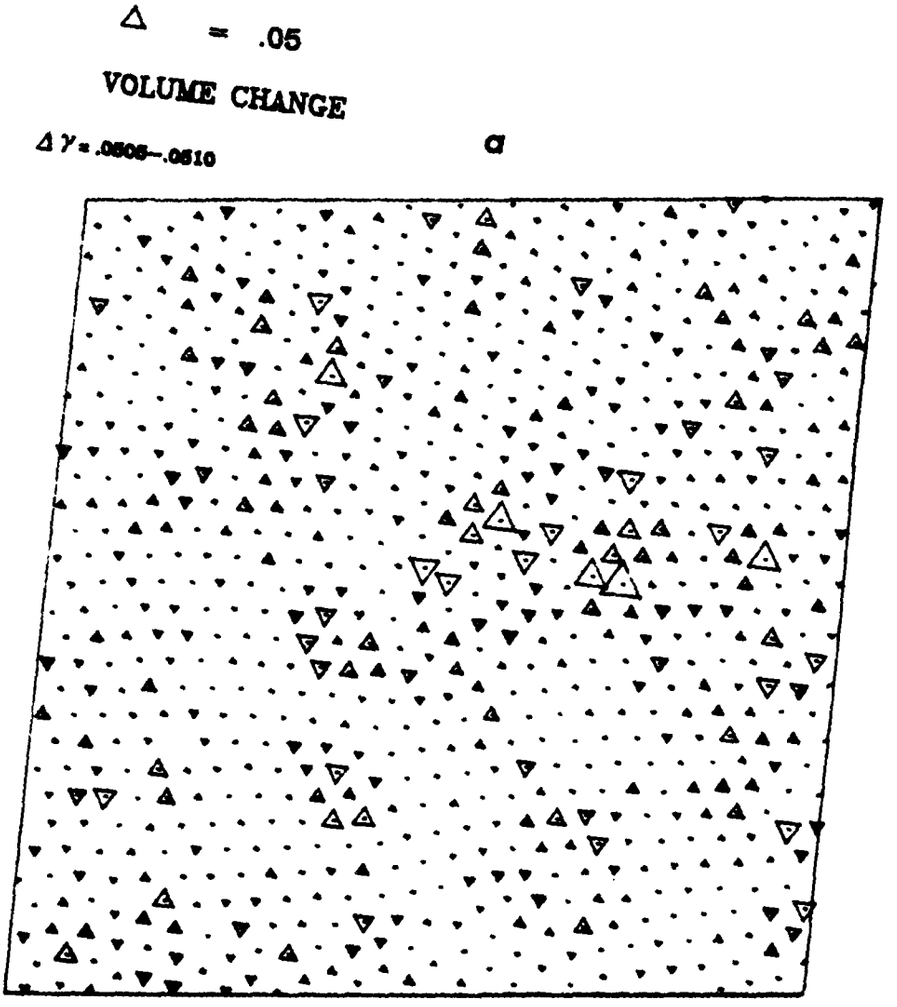

Fig. 22 - Distribution of deformation induced local volume changes during externally imposed strain increments of 5×10^{-4} at total strains of: (a) $\gamma = 0.05$, (b) = 0.10, (c) $\gamma = 0.15$, and (d) $\gamma = 0.20$.

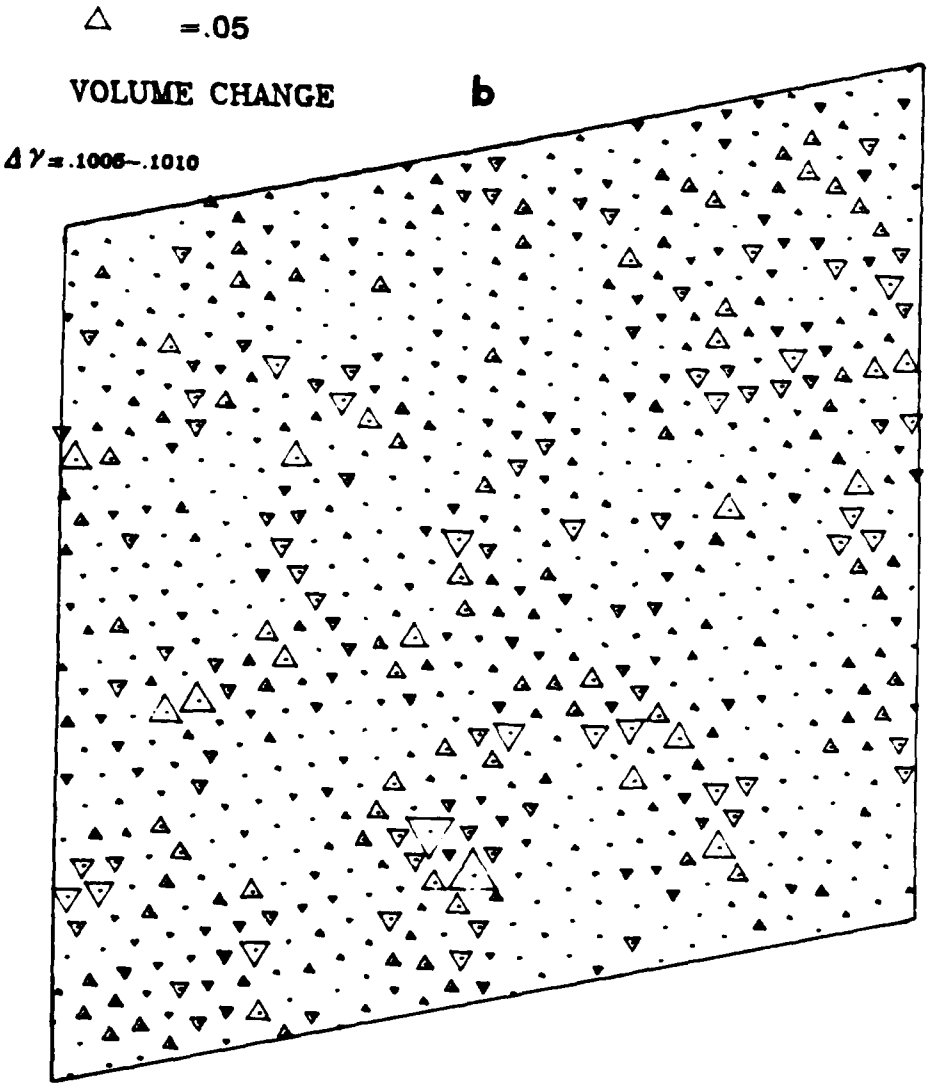

Fig. 22b

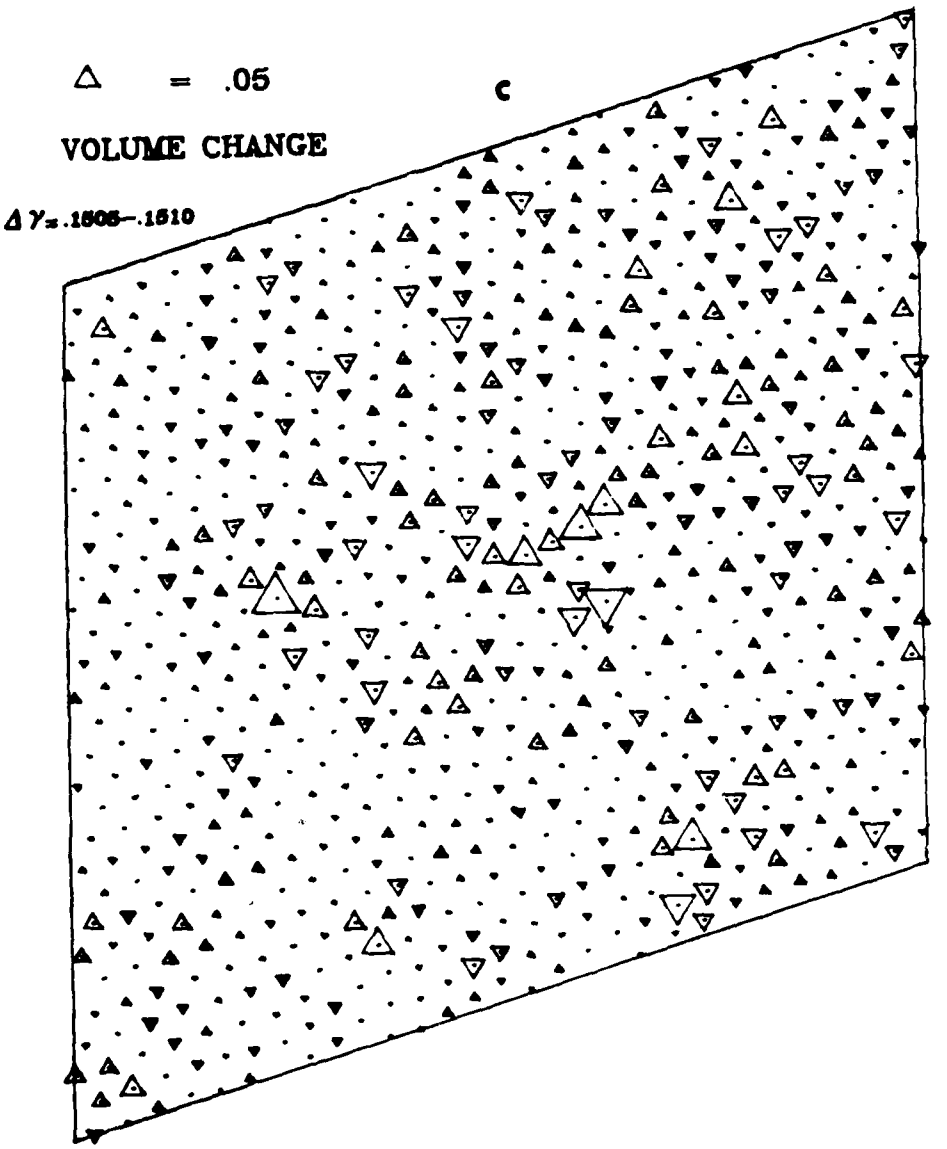

Fig. 22c

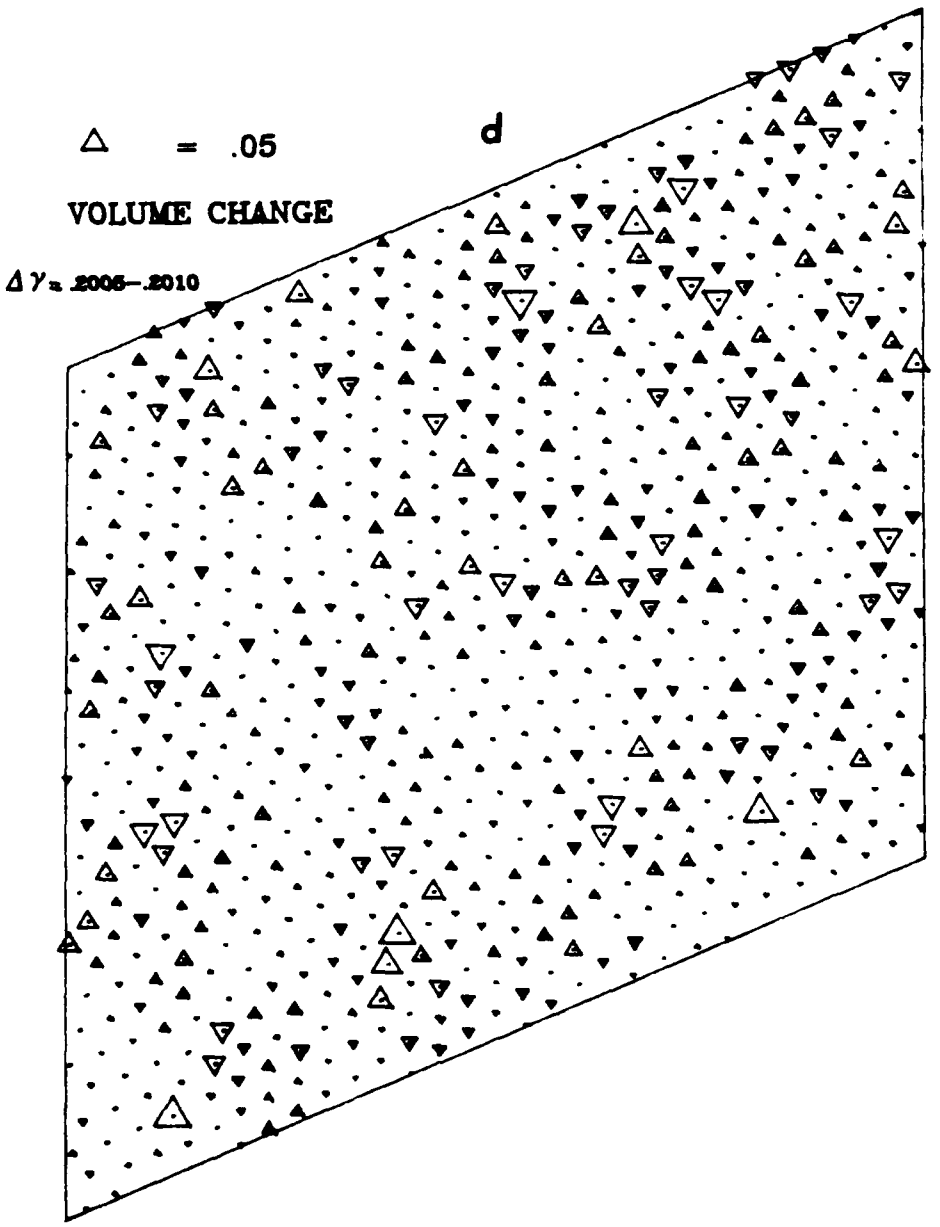

Fig. 22d

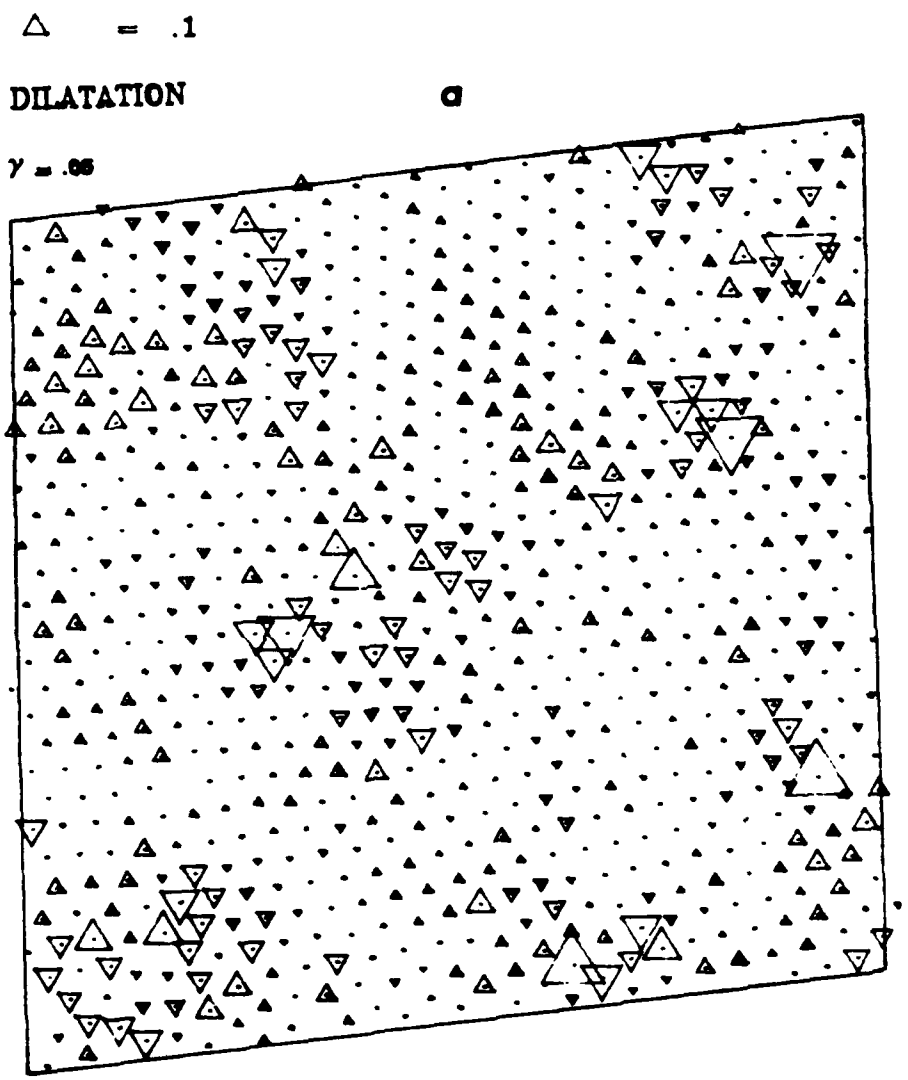

Fig. 23 - Distribution of total accumulated local dilatations at atom sites at total strains of: (a) γ = 0.05, (b) γ = 0.10, (c) γ = 0.15, and (d) γ = 0.20.

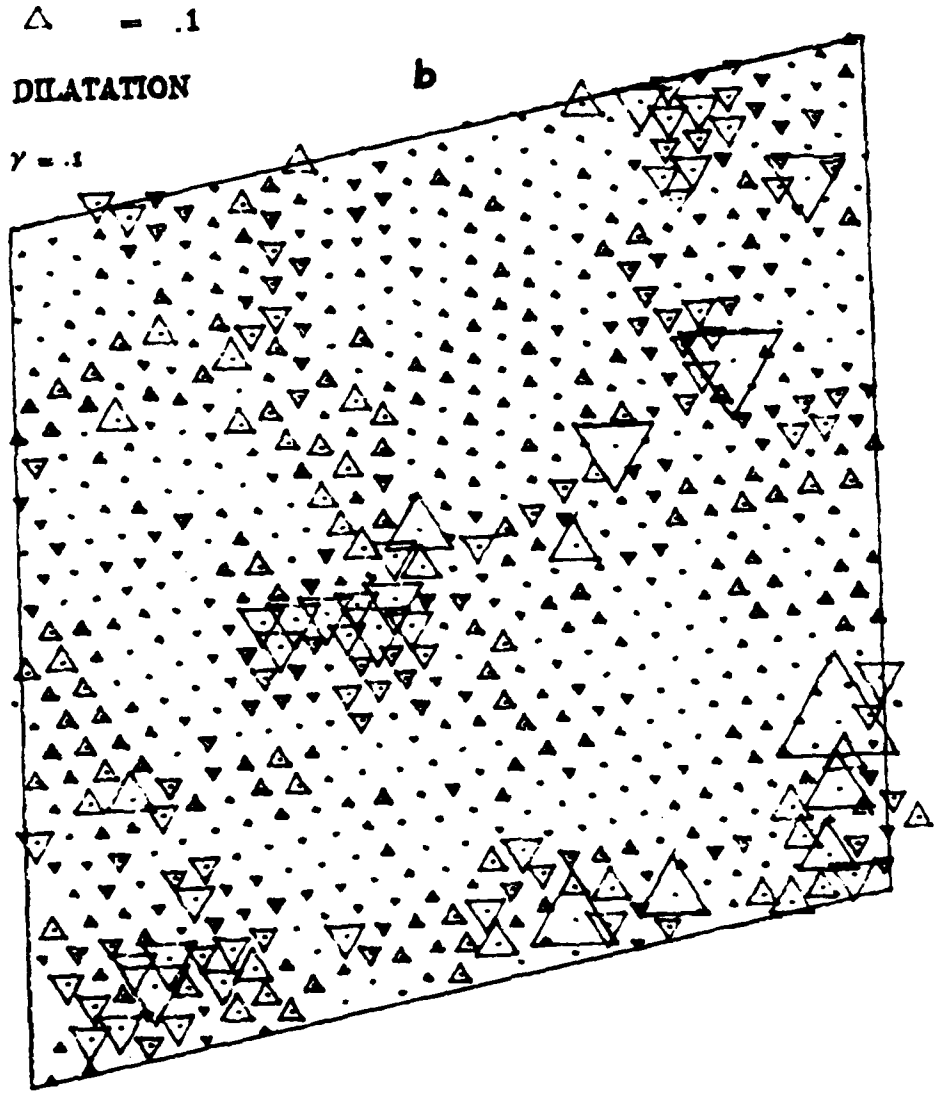

Fig. 23b

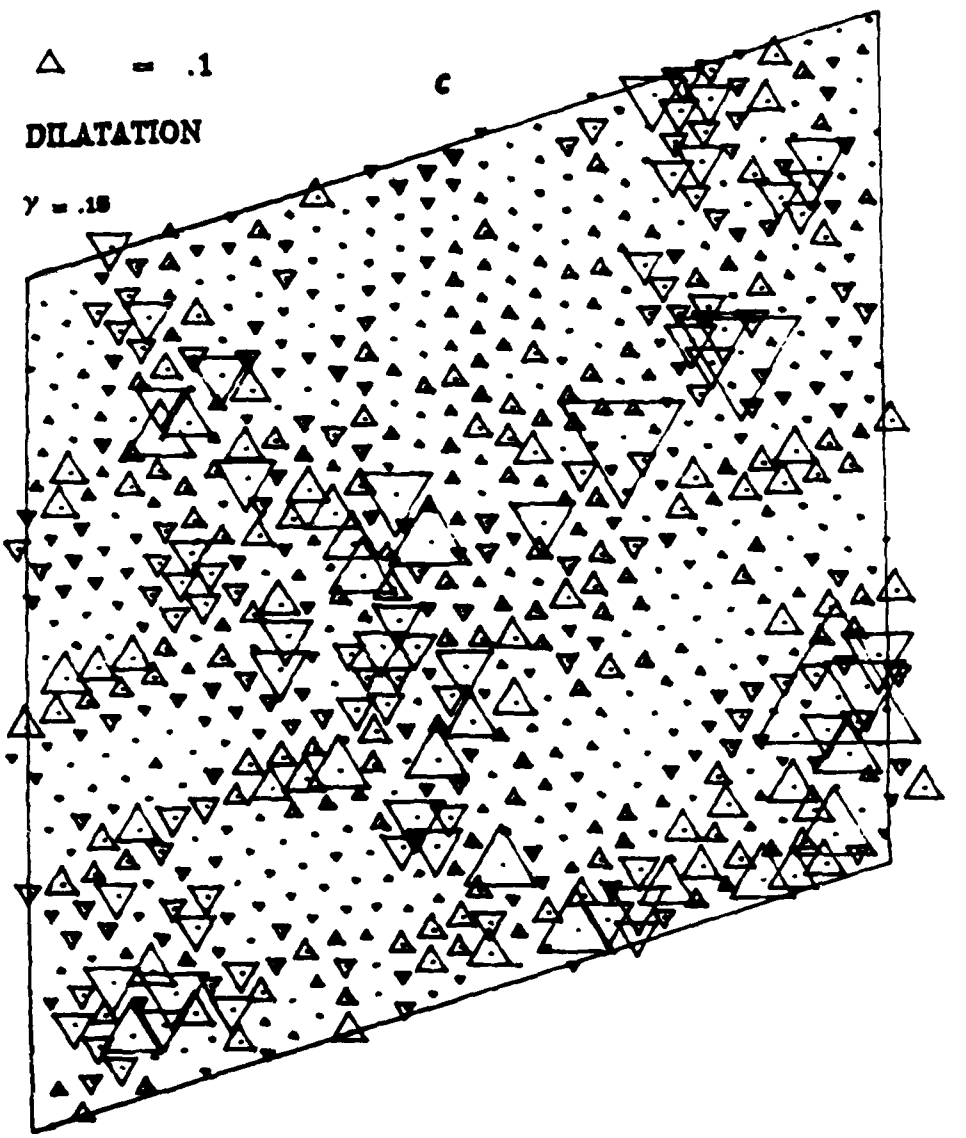

Fig. 23c

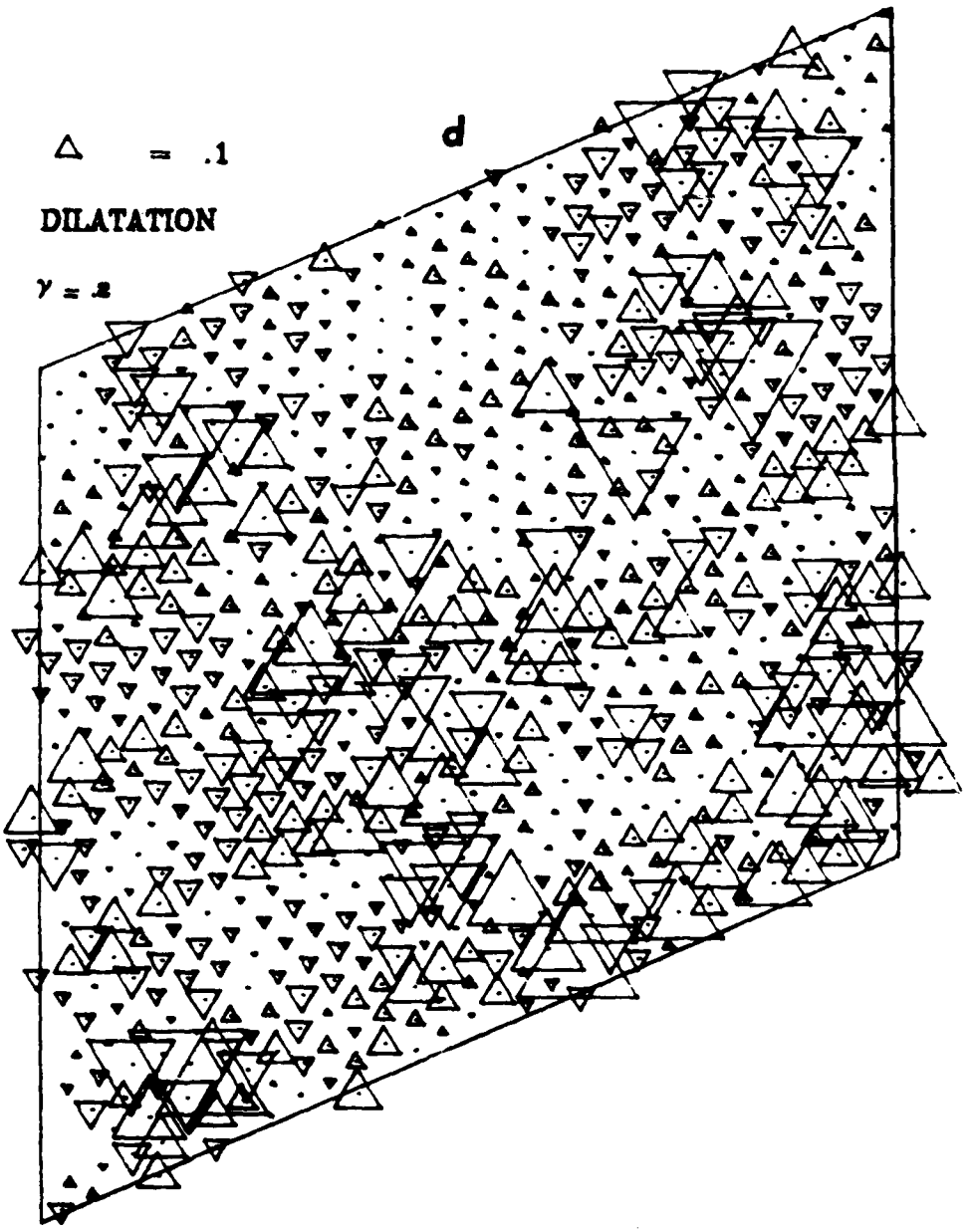

Fig. 23d

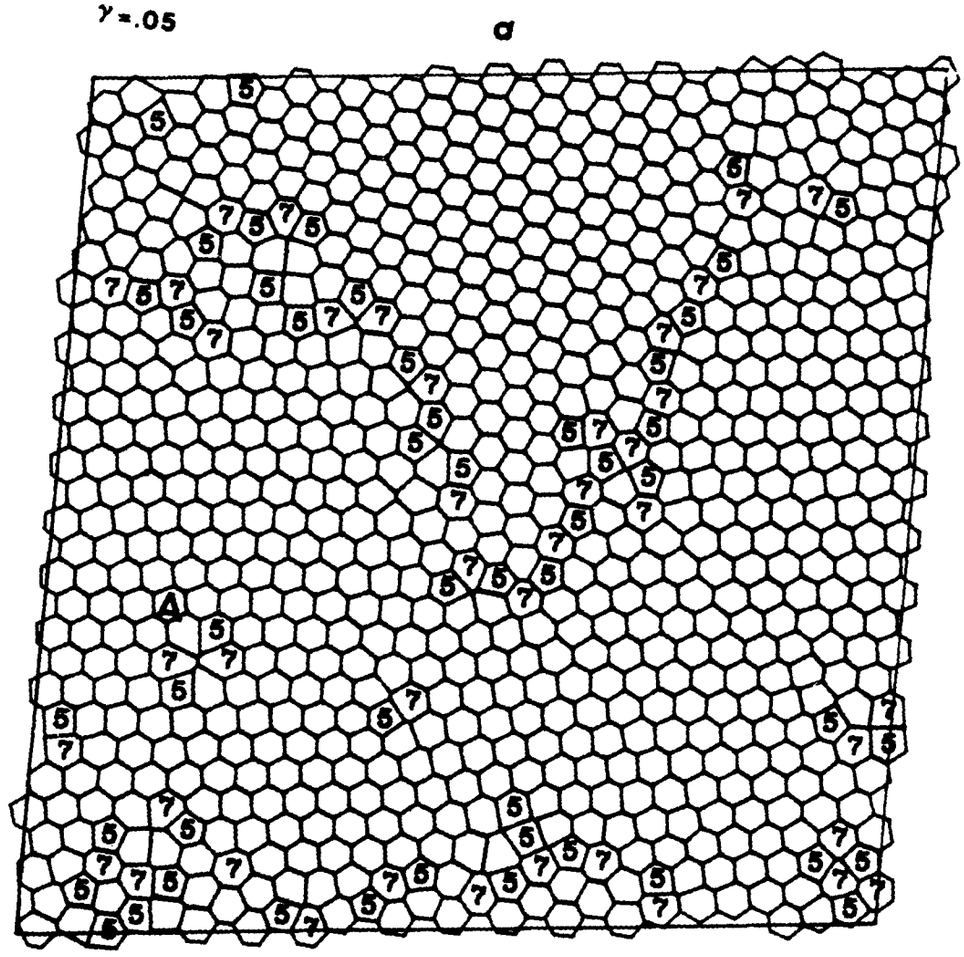

Fig. 24 - Deformation induced changes in the distribution of liquid-like material represented by the boundaries of 5-7 sided polygons: (a) after a total strain of $\gamma = 0.05$, note a dipole of two-edge dislocations at site marked A, (b) after $\gamma = 0.10$, note the separation of the two-edge dislocations from the dipole configuration, (c) after $\gamma = 0.15$, note that the left-hand dislocation has now entered the cell from the right side, (d) after $\gamma = 0.20$.

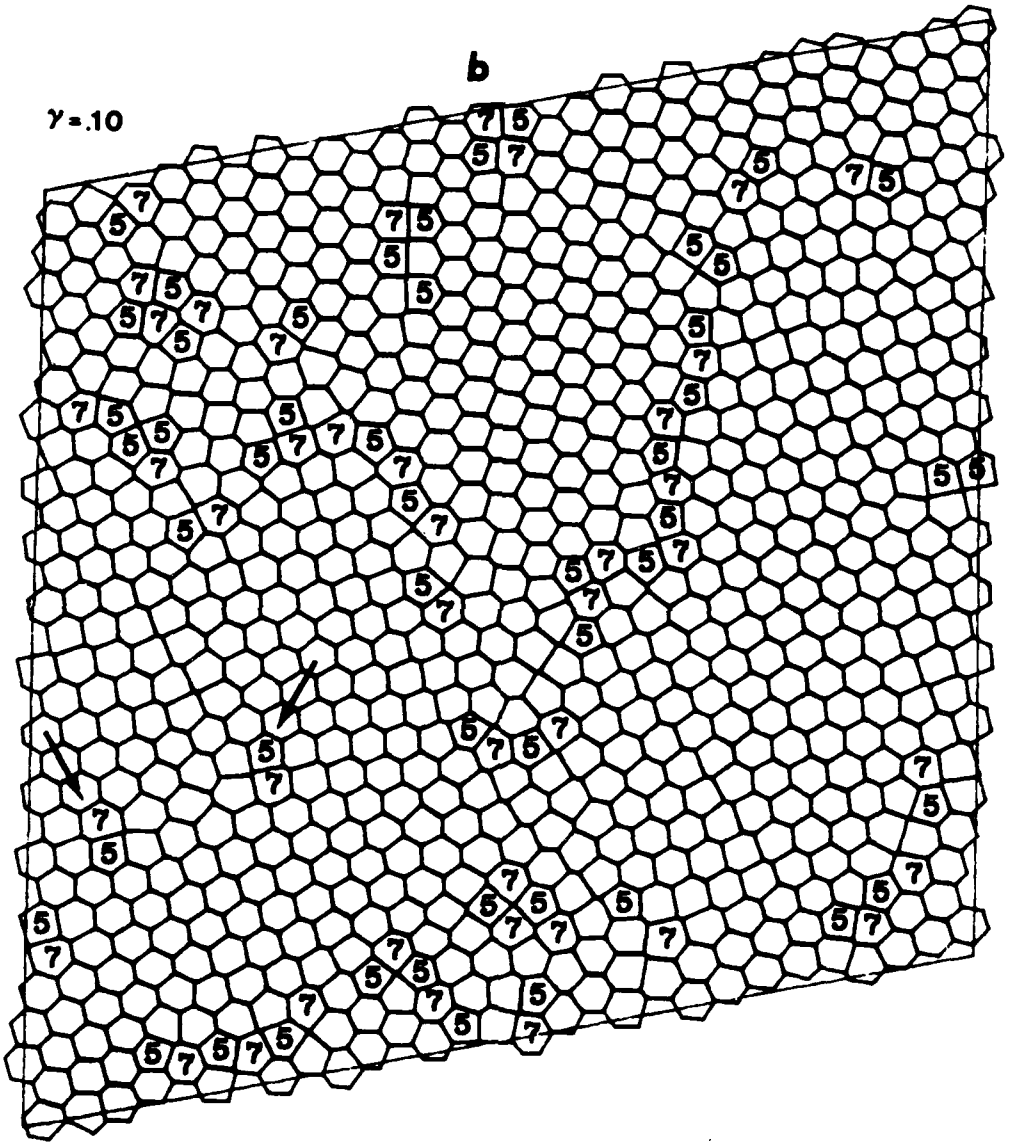

Fig. 24b

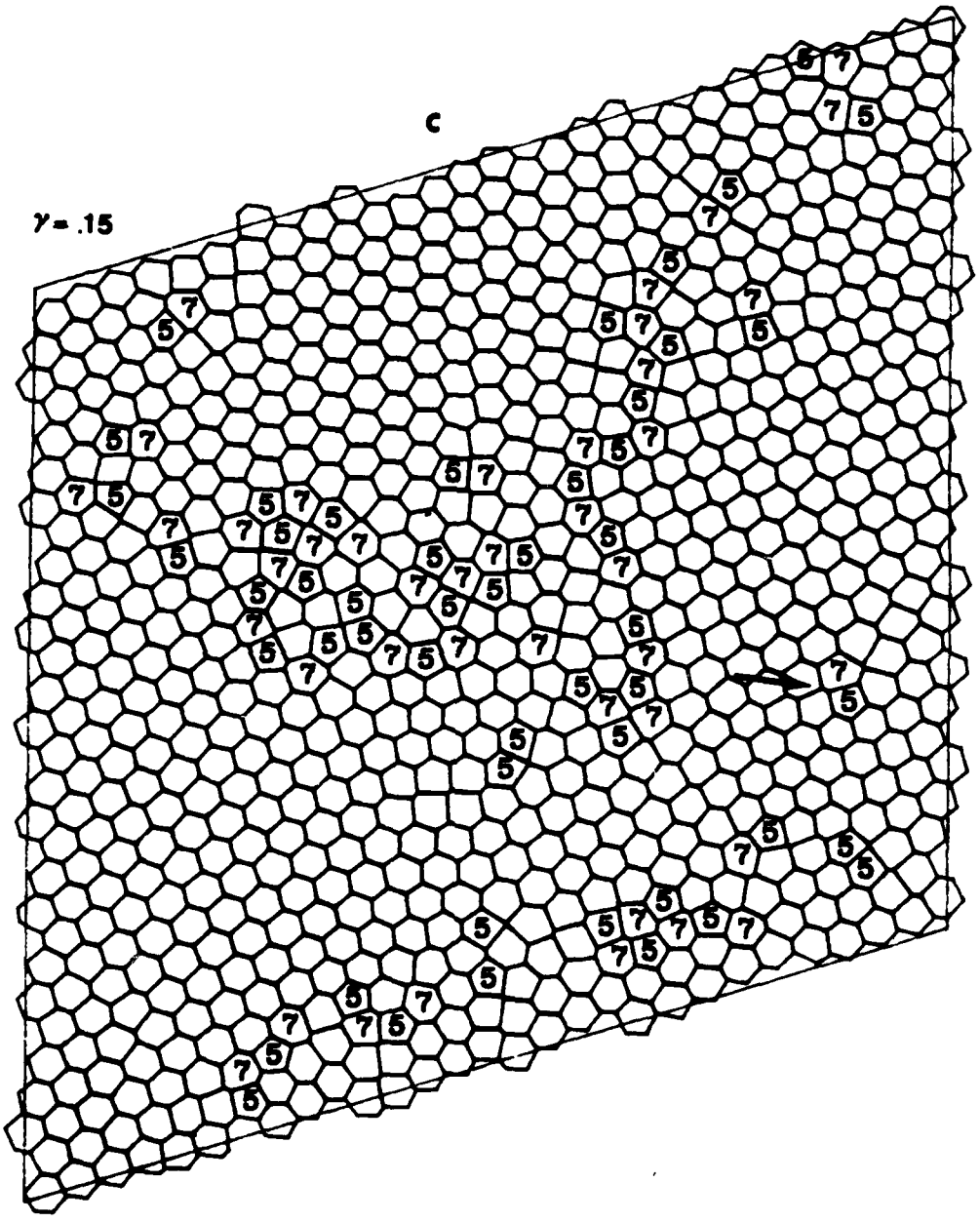

Fig. 24c

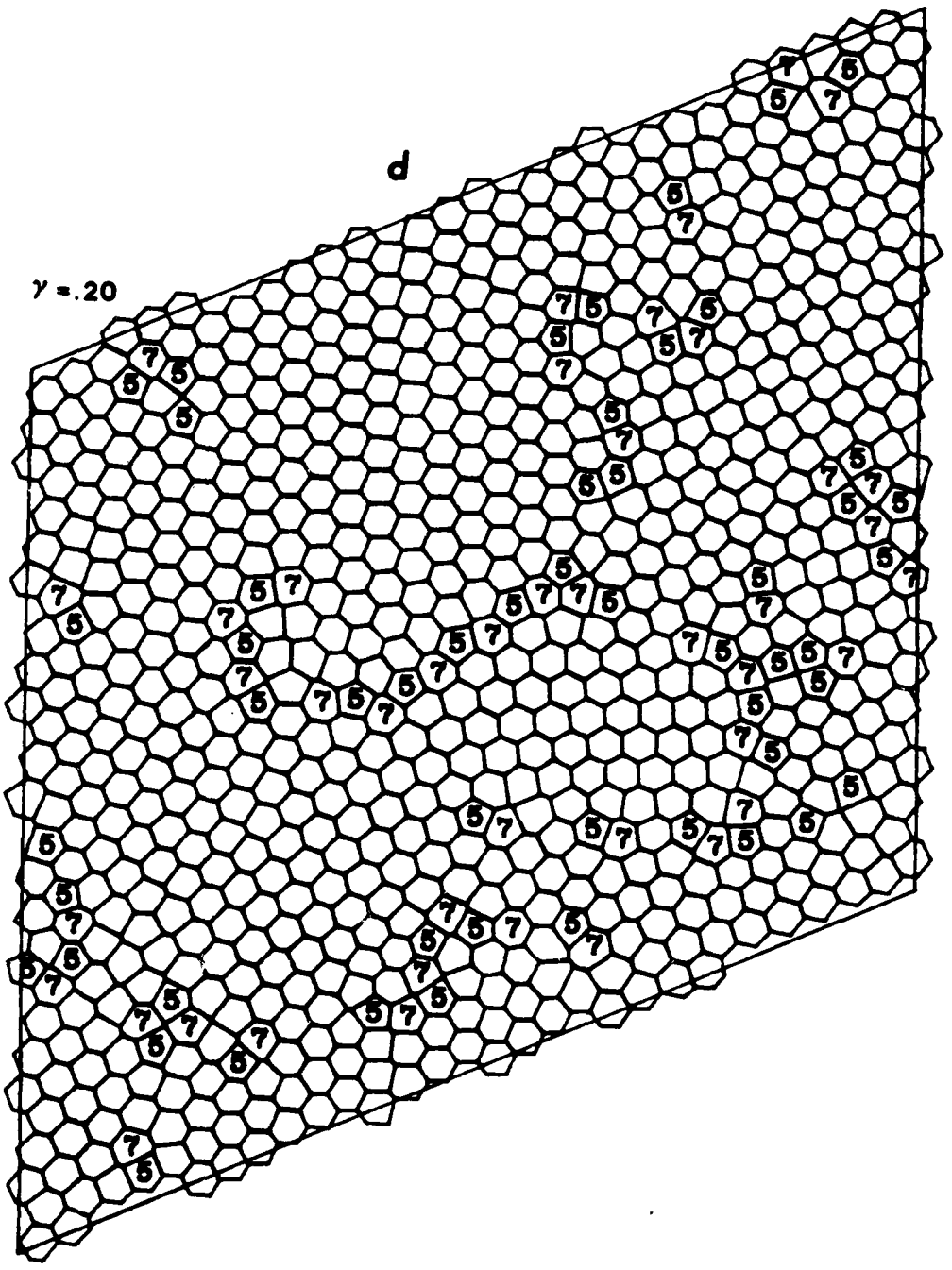

Fig. 24d

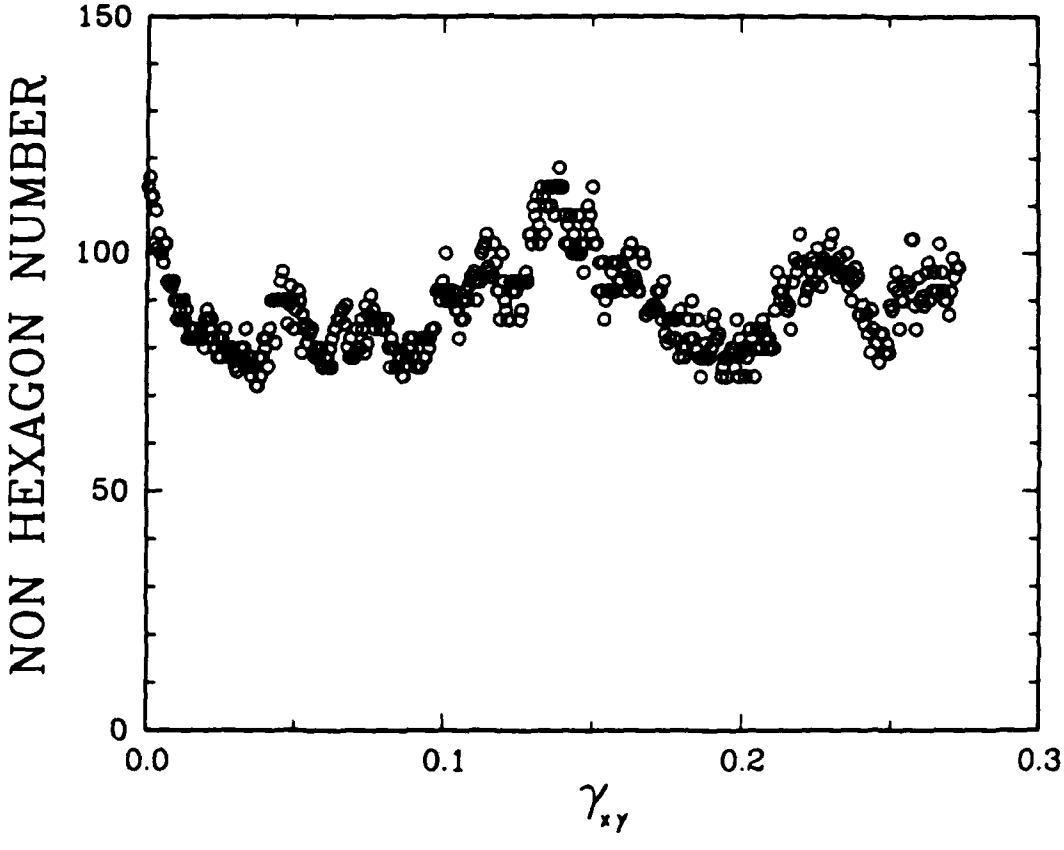

Fig. 25 - Variation with strain of the total number of liquid-like material polygons with edges different than 6.